



University of Cambridge  
Department of Materials Science & Metallurgy

# Modelling of Microstructural Banding during Transformations in Steel

Dipl.-Ing. Eric A. Jäggle  
Pembroke College

August 2007

A dissertation submitted for the degree of Master of Philosophy  
in Materials Modelling at the University of Cambridge



## Abstract

Microstructural banding is defined as alternating layers of two different microstructures in steel, often ferrite and pearlite. It is caused by fluctuations in the concentration of alloying elements, primarily manganese, due to microsegregation introduced during solidification. In this thesis, a model is presented to simulate banding using phase transformation kinetics theory. An existing program that simulates the decomposition of austenite to allotriomorphic ferrite, Widmanstätten ferrite and pearlite upon cooling was significantly modified to treat steels with an inhomogeneous distribution of solute, with the focus on manganese. The concentration profile was divided into discrete concentration steps (“slices”) and paraequilibrium conditions were assumed. The slices interact by the partitioning of carbon between them. After each time step, the concentration of carbon in untransformed austenite is calculated by taking into account the amount of ferrite formed in all slices, effectively assuming infinitely fast carbon partitioning.

Simulations were carried out using three sets of input parameters, one of them being a typical steel with parameters chosen to clearly show banding and two of them taken from the literature for comparison of the model with experimental data. Input parameters were systematically varied to test the behaviour of the program. Trends for varied cooling rate, austenite grain size and concentration fluctuation amplitude are in accordance with the expected results. The model was capable of reproducing the suppression of banding above a critical cooling rate, although this rate did not quantitatively agree with experimental findings for all the test cases implemented. Results differ from experiments mainly for high cooling rates, probably due to the unrealistic assumption of infinitely fast carbon partitioning between the slices. A method is suggested on how the current model could be improved to include a finite carbon partitioning velocity. The work nevertheless represents the most comprehensive treatment of the phenomenon of banding to date.

# Preface

This dissertation is submitted for the degree of Master of Philosophy in Materials Modelling at the University of Cambridge. The research described herein was conducted under the supervision of Professor H.K.D.H. Bhadeshia in the Department of Materials Science and Metallurgy, University of Cambridge, between May 2007 and August 2007.

Except where acknowledgements and references are made to previous work, this work is, to the best of my knowledge, original. Neither this, nor any substantially similar dissertation has been or is being submitted for any other degree, diploma or other qualification at any other university. This dissertation contains less than 15,000 words.

Eric A. Jägle  
August 2007

# Acknowledgements

Firstly, I would like to sincerely thank my supervisor Harry Bhadeshia for many insightful lectures, helpful comments and delicious biscuits at coffee break. It was always a pleasure working with him and he always provided me with prompt help or encouragement whenever I was in need of one of them. If I hadn't done it before, I would certainly understand now how wonderful a material steel is.

I would also like to thank all members of the phase transformation group for warmly welcoming me into the group and for their support with various aspects of my work.

My studies in Cambridge would not have been possible without the generous support of the German Academic Exchange Service and the Dr. Jürgen Ulderup programme of the German National Academic Foundation. I am deeply grateful for the opportunity they gave to me.

Pembroke College has been a place for me where I could feel at home during the last year. Especially the many wonderful friends that I have found there have been both a support for and a distraction from my work. I would like to thank them for both.

Another valuable source of support was my family which has been as encouraging and reassuring as always. I don't take this for granted. Finally, I would like to thank my girlfriend Mareike for her great patience during the last twelve months.

# Contents

<b>Preface</b>	<b>4</b>
<b>Acknowledgements</b>	<b>5</b>
<b>Nomenclature</b>	<b>8</b>
<b>1. Introduction</b>	<b>10</b>
1.1. Banding in Steel . . . . .	10
1.1.1. Mechanism of Band Formation . . . . .	11
1.1.2. Factors Influencing the Development of Banded Microstructures . . . . .	13
1.1.3. Effects of Banding on Mechanical Properties . . . . .	13
1.2. Modelling of Banding . . . . .	15
1.2.1. Microsegregation during Solidification . . . . .	15
1.2.2. Dendrite Arm Distance and Coarsening . . . . .	19
1.2.3. Homogenisation during Heat Treatment . . . . .	19
1.2.4. Effect of Deformation on Segregation Profiles . . . . .	20
1.2.5. Phase Transformations in Segregated Microstructures . . . . .	21
<b>2. The Method</b>	<b>24</b>
2.1. The Model . . . . .	24
2.2. Modifications to the Original Program . . . . .	26
2.3. Input Parameters . . . . .	29
2.3.1. Constants . . . . .	29
2.3.2. “Technical” Parameters . . . . .	30
2.3.3. Varied Parameters . . . . .	35
2.4. Output . . . . .	36
2.5. Accuracy of Calculations . . . . .	37
<b>3. Results and Discussion</b>	<b>38</b>
3.1. The Effect of Various Input Parameters . . . . .	38
3.1.1. Carbon Partitioning . . . . .	38
3.1.2. Cooling Rate . . . . .	38
3.1.3. Austenite Grain size . . . . .	45
3.1.4. Concentration Fluctuation Amplitude . . . . .	47
3.2. Comparison with Results from the Literature . . . . .	49
3.2.1. Test Case “A”: Kirkaldy et al. [1] . . . . .	49
3.2.2. Test Case “B”: Caballero et al. [2] . . . . .	49
<b>4. Conclusions and Further Work</b>	<b>56</b>

<b>A. FORTRAN-Program</b>	<b>58</b>
<b>B. Example Input File</b>	<b>59</b>
<b>Bibliography</b>	<b>60</b>

# Nomenclature

$\alpha$	ferrite
AF	allotriomorphic ferrite
$A_{r3}$	temperature at which ferrite starts forming upon cooling of austenite
$B$	geometry parameter of coarsening
$C_S^*$	concentration of alloying element in solid at the solid/liquid interface
$C_\alpha^*$	carbon concentration in ferrite in equilibrium with austenite
$C_i$	concentration of element $i = \text{C, Mn, Cr} \dots$
$C_j$	carbon concentration in phase $j = \alpha, \gamma \dots$
$C_j^{\text{pe}}$	paraequilibrium carbon concentration in phase $j$
$C_0$	average concentration in the sample
CR	cooling rate
$\Delta C_{\text{Mn}}$	amplitude of the manganese concentration fluctuation
$\Delta t$	time step
$D_C$	diffusion coefficient of carbon in austenite
$D_S$	diffusion coefficient of solute in solid
$D_j$	average grain size in phase $j$
$f_j$	volume fraction of phase $j$
$\gamma$	austenite
$G$	volume growth rate
GB	grain boundary
$g$	geometry factor of growth
$h$	dendrite spacing exponent
$I$	nucleation rate per unit volume
$J$	carbon flux
$k$	equilibrium partition coefficient
$L$	width of the treated system, equals one half of the dendrite arm spacing
MLI	mean linear intercept
$n$	number of discrete concentration steps or "slices"
$n_t$	number of time steps until the current time
$n_k$	total number of planes
$N_{v,\alpha}$	total number of successful ferrite nuclei per unit volume
$N_{j,k}$	total number of nuclei in phase $j$ on plane $k$
$O_B$	total grain boundary area per unit volume
$O_{j,y}$	transformed area of phase $j$ on plane at distance $y$ from the GB
$O_{j,y}^e$	extended transformed area of phase $j$ on plane at distance $y$ from the GB
P	pearlite
$p_i$	parameters
$\sigma, \beta$	arbitrary phases

---

$\theta_f$	local solidification time
$\tau$	incubation time
$t$	time
$T$	temperature
$V_{\text{tot}}$	total volume of the specimen
$V_j$	transformed volume of phase $j$
$V_j^e$	extended transformed volume of phase $j$
$\omega$	segregation coefficient
WF	Widmanstätten Ferrite
$y$	distance of a plane from the grain boundary

# Chapter 1.

## Introduction

### 1.1. Banding in Steel

“Banded microstructure, or *banding*, is the microstructural condition manifested by alternating bands of quite different microstructures aligned parallel to the rolling direction of [hot rolled] steel products.” [3, p. 169] In many cases these bands consist of ferrite and pearlite, but this is not always the case. Banded microstructures of ferrite and martensite, ferrite and bainite, two kinds of bainite, high-cementite and low-cementite and other combinations are known [4]. An example of a micrograph showing a banded microstructure is given in figure 1.1 (a). The earliest works on banding date back to the beginning of the last century [5–7] and papers are still being published. In fact, Verhoeven describes banding in his recent review as an “ubiquitous microstructure” [4]. Another review paper was recently published by Krauss [8].

The origin of banding lies in the solidification process. Consider a liquid steel with one alloying element besides carbon and a relatively low concentration of this alloying element. The chosen alloying element lowers the melting point of iron. Thus, the composition of the first crystallites to form (given by the solidus line of the phase diagram) is lower in solute than the remaining liquid. The alloying element is rejected by the growing crystal. As the temperature decreases, the equilibrium phase diagram predicts that the content of solute in the solid phase grows steadily until, when the last drop of liquid solidifies, the whole material possesses a uniform composition again. At typical cooling rates, however, solid state diffusion is not fast enough to completely equilibrate the composition of the material once it is solid. Therefore, a material with an inhomogeneous chemical composition results. This process is called microsegregation, because it happens on the length scale of individual grains (as opposed to macrosegregation, which happens on the scale of the whole specimen). The morphology of grains grown under usual cooling conditions is dendritic (greek for “treelike”). The concentration of solute inside dendrites will be lower than that in the interdendritic regions. Details of microsegregation are discussed in section 1.2.1.

During a following heat treatment, partial or complete homogenisation may occur, but due to the relatively low diffusivity of substitutional alloying elements in steel, the removal of microsegregation patterns requires long high-temperature annealing (cf. section 1.2.3). When the material is hot rolled, the form of the concentration profile changes according to the plastic deformation of the material. Interdendritic regions that are low in solute that were elongated are flattened and the resulting structure consists of alternating layers of high and low solute content. During cooling after hot deformation, the austenite to ferrite phase transformation takes place. Supposing the steel is of hypoeutectic composition, ferrite will form in the regions of the sample with low austenite-stabilising alloying element content. The rest of the austenite decomposes to pearlite, leading to the aforementioned layered or banded microstructure. The processes that lead to banding are summarised in a flowchart (figure 1.1b) and an example for the concentration profile in a banded microstructure is shown in figure 1.2.

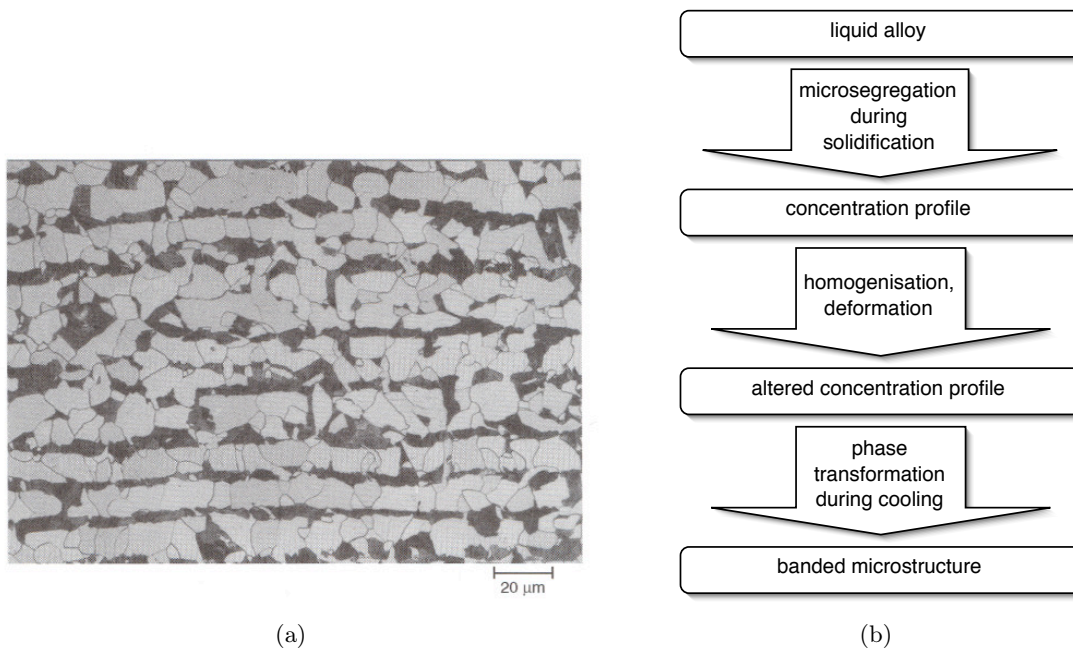


Figure 1.1.: (a) An example of a banded microstructure in 1020 steel consisting of ferrite (light) and pearlite (dark) [3] and (b) a flowchart illustrating the processes leading to banded microstructures.

### 1.1.1. Mechanism of Band Formation

In an important publication from 1962, Kirkaldy and co-workers determined which mechanism leads to the evolution of bands of different phases [1]. It had been known that banding coincides with chemical microsegregation because segregation patterns can be made visible with special etching techniques [5, 6], but it was not clear how segregation gives rise to banding. Two different mechanisms had been proposed by Jatzcak et al. [10] and Bastien [11] that Kirkaldy calls “presegregation” and “transsegregation”.

Presegregation means that the differences in carbon concentration present *before* the phase transformation are responsible for the location where hypoeutectoid ferrite forms. Segregated alloying elements either lower or raise the activity of carbon in iron. Because carbon diffuses rapidly at temperatures at which austenite is stable, it is in equilibrium (i.e. its activity is the same) everywhere in the sample. Regions where the equilibrium concentration of carbon is low (due to an elevated carbon activity) are more likely to yield ferrite nuclei than those in which carbon concentration is elevated due to a lowered activity.

Transsegregation assumes that the effect of presegregation is negligible. Instead, the effect of alloying element concentration on the local  $A_{r3}$  temperature (the temperature at which ferrite starts to form from austenite upon cooling) determines where ferrite is nucleated first. In regions with a high content of elements that increase the  $A_{r3}$  temperature (ferrite stabilisers), ferrite nuclei will form earlier (i.e. at higher temperatures) than in regions with a high content of austenite stabilisers. Ferrite stabilisers are for example phosphorus or silicon while manganese, nickel and chromium are austenite stabilisers.

To determine which one of these mechanisms dominates the formation of bands, Kirkaldy et

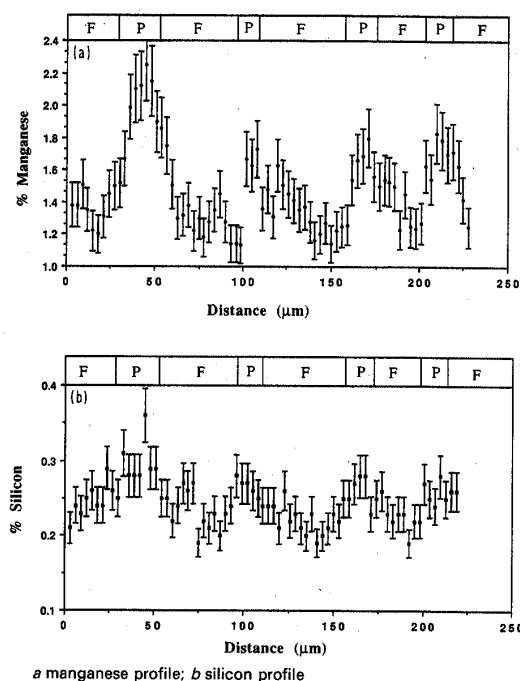


Figure 1.2.: Typical concentration profiles in a banded steel. Above the profiles, the corresponding microconstituent is noted. F stands for proeutectoid ferrite and P for pearlite. [9]

al. simulated a segregated microstructure by welding a disc of alloyed steel (with various alloying elements) between two discs of plain carbon steel with the same carbon content. After a heat treatment, the microstructures were analysed by light microscopy to detect in which part of the sample ferrite formed first. Of particular importance was the analysis of the sample with nickel as alloying element. Nickel lowers the  $A_{r3}$  temperature which would lead to ferrite bands in the plain carbon steel according to the transsegregation hypothesis, but it also raises the activity of carbon which would lead to faster ferrite nucleation in the alloyed steel according to the presegregation hypothesis. The experiment showed that the former is the case and therefore the transsegregation hypothesis is validated. Experiments with manganese, silicon, chromium and phosphorus assist this result.

A slightly different mechanism applies to steels with a noticeable sulphur content. Kirkaldy et al. [12] analysed a steel with manganese and sulphur as alloying elements. Ferrite surprisingly formed in the manganese-rich areas. This was explained by the growth of MnS inclusions in these regions that drain Mn from the matrix thus creating a low-manganese region around the inclusions where ferrite first nucleates. Experimental evidence for this is given by Turkdogan and Grange [13]. The diffusion profile of manganese around a growing MnS inclusion has been calculated by Enomoto [14] showing that Mn depletion occurs at a significant level. The presence of inclusions generally complicates the analysis of banding in steels and early work (cited in [4]) even falsely attributed banding to the presence of sulphide inclusions (discussion in section 1.1.3).

### 1.1.2. Factors Influencing the Development of Banded Microstructures

The cooling rate applied after the austenitisation of a steel plays a crucial role in the development of its microstructure. Under slow cooling conditions, a banded ferrite/pearlite microstructure results. If the cooling rate is fast, however, there is not enough time for carbon diffusion and ferrite nucleation and no banded microstructure results [2, 15]. In figure 1.3(a) one can see that banding is much less pronounced in the sample that was taken from the edge of a hot rolled sheet where the cooling rate is higher than in the centre of the sheet. Quenching finally leads to a homogeneous martensitic microstructure [16]. While fast cooling can suppress the formation of a banded microstructure, it cannot remove the reason for banding, i.e. the microsegregation. Therefore, if a specimen with suppressed banding is reheated and cooled slowly, bands reappear [15]. The fact that a faster cooling rate shortens the carbon diffusion length was demonstrated by Turkdogan and Grange [13] who observed that the band width decreased with increasing cooling rate.

By holding in the austenite-ferrite two-phase region and subsequent fast cooling, banded ferrite/martensite microstructures can be obtained [17]. Tomita [18] describes a similar heat treatment including water cooling that leads to ferrite/bainite banding. On the other hand, annealing at high temperatures leads to the removal of bands. Grange [19] reports that a 10 minute treatment at 1315 °C removes banding in a 1.5wt.-% Mn steel, but not microsegregation: After hot rolling the bands reappeared. It takes a considerably longer time to remove microsegregation and thereby the reason for banding. Owen et al. [16] showed that banding is not completely removed after annealing a 0.7wt.-% Mn steel for one hour at 1250 °C and Jateczak et al. [10] still observed martensite/pearlite banding in 4340 steel after 200 h at 1200 °C. Such long high-temperature heat treatments are not economically feasible and banding can therefore often not be avoided.

Another factor that influences banding is the austenite grain size. Thompson and Howell [9] discuss this parameter in detail. Ferrite grains nucleate at austenite grain boundaries. If the austenite grains are small compared with the wavelength of microsegregation, sufficient nucleation sites are present and ferrite will nucleate in regions of low manganese concentration. Ferrite grains will grow along isoconcentration lines until they impinge, after which they grow perpendicular to the bands leading to a “bamboo” structure. The rest of the austenite transforms to pearlite. Figure 1.3(b) illustrates this process. If the austenite grains are much larger than the microsegregation wavelength, however, there are not enough nucleation sites for ferrite available and banding is not possible. Thompson and Howell [9] and Verhoeven [4] cite many experimental works that agree with this reasoning.

### 1.1.3. Effects of Banding on Mechanical Properties

The effect of banding on the mechanical properties of steel have been studied by means of tensile, hardness and impact testing. Tensile properties such as yield strength and ultimate tensile strength are only weakly affected by banding [20], but Grange [19] noted that the reduction in area was lowered with respect to an unbanded microstructure, hinting to a lower ductility. There are differing views expressed in the literature whether impact properties change with the degree of banding. Sakir Bor [20] noted that the Charpy impact energy decreased with increasing banding, while the material became more anisotropic. Owen et al. [16] found no difference in the Charpy impact energy for brittle fracture, but they noted an influence in the ductile range. A thorough study in the impact properties of a microalloyed steel by Shanmugam and Pathak [21] shows that the upper shelf energy (i.e. the impact energy in the ductile range) decreases with increasing

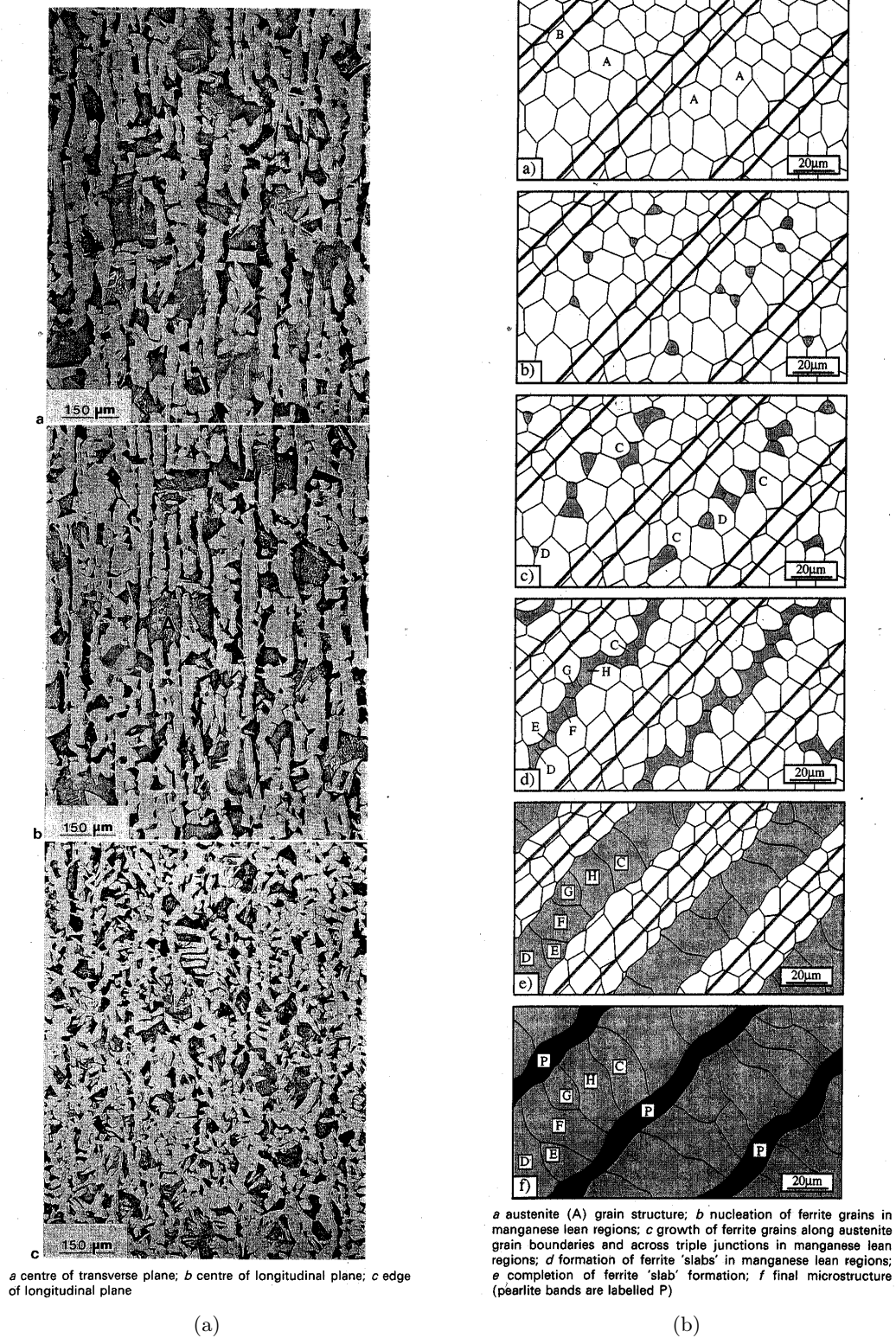


Figure 1.3.: Two figures from Thompson and Howell [9], (a) showing optical micrographs of specimens taken from different locations of a hot rolled steel sheet. The steel contained 1.5 wt.-% Mn and 0.15 wt.-% C. (b) Illustration of the growth processes leading to banding.

number of bands per unit area, while the ductile-to-brittle transition temperature is lowered. This last observation was explained with the operation of a delamination mechanism. Banded microstructures are also less susceptible to fatigue cracking because the layered microstructure favours crack branching [22]. Fractographic investigations by Tomita [18] similarly show that the improved ductility of banded steel is due to crack arresting mechanisms in ferrite bands.

There are two flaws in most investigations on the mechanical properties of banded materials. Firstly, the band width often varies strongly between the specimens of a study. Secondly, the influence of MnS inclusions is often not assessed independently from the presence of banding. Krauss [8] addressed the first problem by measuring the mechanical properties of artificially banded structures with varying band width. It was shown that ductility improves with decreasing band width while yield and tensile strength decrease. The second problem was solved by Spitzig [23]. He studied three different steels, one with low sulphur content and therefore few inclusions, one with “stringered” sulphide inclusions and one with inclusions of globular shape due to the addition of rare earth metals. Banding in these steels could be removed by a short high-temperature treatment without affecting the shape and number of the inclusions. Spitzig concluded that, under these circumstances, banding had no effect whatsoever on tensile or impact properties, while the shape and number of the inclusions had a large influence.

From these results it becomes clear that it is not easy to make judgements regarding the mechanical properties of banded materials. Often, other factors such as grain size and inclusion density that are not considered in the experiments are the true reason for a change in properties.

## 1.2. Modelling of Banding

To predict the banding behaviour of steel, it is necessary to choose and apply several models. The flowchart in figure 1.1(b) lists all steps. Firstly, the microsegregation during solidification must be modelled. Input parameters are the chemical composition of the studied alloy and cooling conditions and the output of the model is a segregation profile. Next, the influence of further heat treatments and of mechanical deformation must be taken into account. Therefore, models for homogenisation and deformation are needed. Again, the only input should be the process parameters (temperature, cooling rate, deformation) as well as the initial segregation profile. The resulting segregation profile is in turn used as input for a model that predicts the microstructure for given process parameters. In principle, it should be possible to simulate the expected microstructure with no other information than the composition and process parameters. In the following sections, existing models for all these steps are presented.

### 1.2.1. Microsegregation during Solidification

#### Classic Models

In section 1.1 it was explained that the lever rule does not hold under usual solidification conditions, because cooling is too fast for complete solid state diffusion. The easiest approximation to this problem one can think of is to completely neglect solid state diffusion. This was done in 1942 by E. Scheil [24]. He is usually attributed to be the first who attempted to model segregation during solidification<sup>1</sup>. The problem is reduced to one dimension by considering only a volume

<sup>1</sup>This is subject to some debate. Scheil himself states that his equation is just a generalisation of a theory developed by E. Scheuer in 1931. He also cites a work by J.M. Gulliver from 1913 that apparently comes to the same conclusion. Some authors therefore call equation (1.2) Scheil-Gulliver equation.

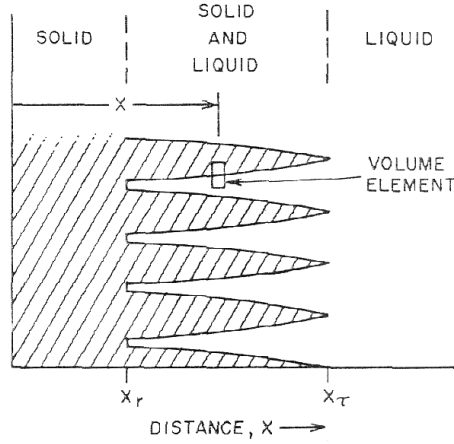


Figure 1.4.: Schematic representation of growing dendrites with the volume element that is considered in the models by Scheil and Brody and Flemings.[25]

element perpendicular to the growth direction of the dendrite (see figure 1.4). The shape of the dendrite is assumed to be plate-like. Further assumptions in this model are infinitely fast diffusion in the liquid state, no undercooling, no difference in density between solid and liquid and linear solidus and liquidus lines. The last assumption leads to a constant equilibrium partition coefficient  $k$  which is given by the ratio of the equilibrium solidus concentration to the equilibrium liquidus concentration (see figure 1.5(a)).

$$k = C_S/C_L \quad (1.1)$$

The Scheil equation describes the concentration at the solid-liquid interface  $C_S^*$  for a given fraction solid  $f_S$  and partition coefficient.

$$C_S^* = kC_0(1 - f_S)^{k-1} \quad (1.2)$$

$C_0$  here is the average concentration of the material. The dependence of  $C_S^*$  on the fraction solid is shown for several models in figure 1.5(b). Of course, this model overestimates the severity of microsegregation. It gives however, together with the lever rule, the lower and upper limit of possible segregation profiles.

In 1966, Brody and Flemings [25] published an improved model that took solid-state diffusion into account. It uses the same geometry and approximations as the Scheil model (with the exception of non-zero diffusion in the solid). Diffusion is described by Fick's second law and two different interface velocity dependencies are assumed: constant velocity and parabolic growth. By assuming that solid state diffusion does not change the concentration gradient at the interface, the interface concentration as a function of the fraction solid can be calculated. The coefficient  $\omega$  is defined as the ratio of the diffusion coefficient in the solid state,  $D_S$  times the local solidification time  $\theta_f$  to the width of the considered system  $L$  squared. The local solidification time is the time from the onset of solidification until all material is solid and therefore inversely proportional to

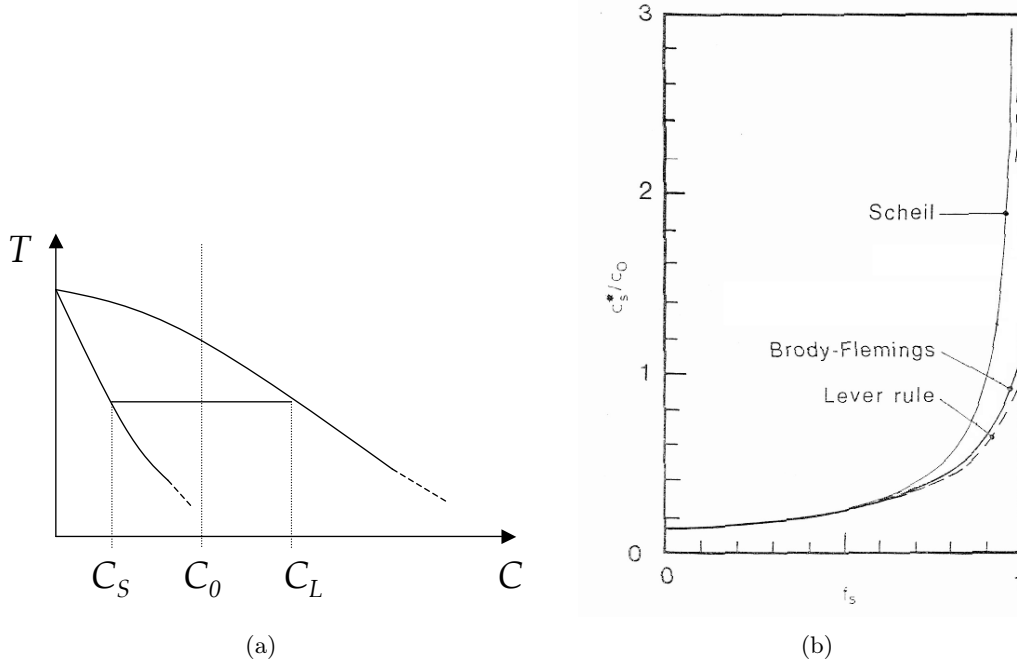


Figure 1.5.: (a) an example partial phase diagram showing the solidus and liquidus concentrations  $C_S$  and  $C_L$  for a given average concentration  $C_0$  (b) The dependence of the concentration at the solid-liquid interface  $C_S^*$  on the fraction solid  $f_S$  for different segregation models (after [26]).

the cooling rate. The width  $L$  is taken to be 1/2 of the dendrite spacing.

$$\omega = \frac{D_S \theta_f}{L^2} \quad (1.3)$$

For a constant solidification velocity, the interface concentration is given by

$$C_S^* = kC_0 \left[ 1 - \frac{f_S}{1 + \omega k} \right]^{k-1}, \quad (1.4)$$

which reduces to the Scheil equation for  $\omega k \ll 1$ . For parabolic kinetics,

$$C_S^* = kC_0 [1 - (1 - 2\omega k) f_S]^{\frac{k-1}{1-2\omega k}} \quad (1.5)$$

holds. It is worth noting that the severity of microsegregation only depends on the ratio of  $\theta_f$  to  $L^2$  and not on one of the parameters alone. Obviously, the cooling rate influences the dendrite spacing, but this model is not able to predict this behaviour.

Even though the Body-Flemings model was a major improvement of the Scheil theory, it still is very limited. Since the 1960s, dozens of models were proposed to overcome the limitations of the two earliest models. Various review articles [26–31] summarise the attempts to model microsegregation.

Improvements that were made include:

- dendrite geometry: cylinders, hexagons and other 2-D geometries
- peritectic solidification with two moving phase boundaries
- finite diffusion or convection in the liquid state
- differences in density between solid and liquid
- undercooling at the dendrite tip
- non-constant partition coefficient (i.e. a realistic phase diagram)
- various cooling conditions such as constant heat flow or input of an experimental cooling curve

Because there are literally hundreds of papers cited in the review articles mentioned above, a comprehensive discussion of the available models for microsegregation cannot be given. However, two models will be described as examples for improvements to the Brody-Flemings model. Roósz and co-workers published a model [32, 33] that combines the calculation of microsegregation with a coarsening model (cf. next section). Diffusivity in the liquid is assumed to be infinite and undercooling is neglected. The heat flow out of the sample is proportional to the difference between the sample temperature and the ambient temperature. Equations for heat flow, diffusion (Fick's 2nd law) and mass balance are solved simultaneously using a finite-difference scheme. Apart from experimental values as  $D_S(T)$  or the phase diagram that are used as input, there is only one parameter (geometry parameter of coarsening  $B$ ) needed to completely describe the model. In [33], calculated values are compared with experiments on Al-Cu-alloys and good agreement is found.

Howe and Kirkwood [34] consider peritectic solidification. This is more complicated than solidification terminated by a eutectic, because two moving phase boundaries have to be considered. When a material with a concentration higher than the peritectic composition solidifies, the first crystals will form as, say,  $\sigma$  crystals. at the peritectic temperature, while a part of the material is still liquid, the peritectic reaction  $\sigma + liquid \rightarrow \beta$  begins and from this temperature onwards, liquid will solidify to  $\beta$  crystals. Because of the limited diffusivity in the solid state, the peritectic reaction cannot take place instantaneously. It gives therefore rise to a  $\sigma/\beta$ -interface that moves through the crystal additionally to the moving  $\beta/liquid$ -interface. Howe and Kirkwood describe several previous approaches to this problem and present a solution by solving all relevant diffusion equations and mass balances using a numerical scheme. They assume a constant cooling rate and infinitely fast diffusion of carbon. Their calculated values for the liquidus and the peritectic temperature agree well with experimental findings, but the solidus temperatures are underestimated, possibly due to neglected undercooling.

### Modern Numerical Models

Even though some of the models mentioned in the previous section are highly sophisticated, they all lack a realistic description of the microstructure. They are either unidimensional or assume very easy two dimensional geometries. With the advent of powerful computers and appropriate modelling techniques, new models for microstructure evolution could be developed. Among the techniques that are frequently used are cellular automata, the phase field method (e.g. [35]) and

front-tracking methods [36, 37]. It is also better possible to integrate models for homogenisation or coarsening into solidification models [37]. It is however beyond the scope of this short survey to thoroughly review all existing models.

### 1.2.2. Dendrite Arm Distance and Coarsening

As we have seen, there are many models available that allow the calculation of the shape of the microsegregation profile and also its amplitude. The wavelength, however, is governed by the distance between two dendrite arms that evolves during during solidification. Verhoeven [4] cites an article by Grange [19] and states that from micrographs therein it is clear that band width corresponds to the spacing of primary dendrite arms. Grange himself however doesn't draw this conclusion and most other authors use *secondary* dendrite arm spacing as the most important measure of the scale of interdendritic segregation (e.g. Krauss [8]).

Both primary and secondary dendrite arm spacing are dependent on cooling rate, but not in the same way [38]. Experiments show that there is an exponential relationship of the form

$$\lambda = \lambda_0 \theta_f^h \quad (1.6)$$

between the secondary dendrite arm spacing  $\lambda$  and the local solidification time  $\theta_f$ , with exponents  $h$  ranging from 0.3 to 0.6.  $\lambda_0$  is an empirical parameter. This holds for many orders of magnitude [8, 39, 40]. The final dendrite spacing is mainly dependent on the coarsening kinetics and not on the initial distance. This was found experimentally by Kattamis et al. [41] and later Roósz et al. [33] confirmed this by using their coarsening model with different initial spacings. Feijóo and Exner [40] give an overview of all proposed mechanisms for dendrite coarsening. The driving force for coarsening is the reduction in solid-liquid interface area. Smaller dendrite arms therefore "remelt" either axially or radially while larger arms grow. The simplest models assume that the driving force for coarsening is inversely proportional to the dendrite arm spacing (which is in turn inversely proportional the curvature). This reasoning leads to an equation that is analogous to Ostwald ripening [33, 41].

$$\lambda(t) = p_1 t^{1/3} \quad (1.7)$$

Here,  $t$  denotes the time and  $p_i$  are empirical parameters. Kirkwood [42] (following Feurer and Wunderlin [43]) derives a slightly different equation by assuming that the concentration in the liquid phase varies linearly with time.

$$\lambda(t) = p_2 \ln(1 + p_3 t) \quad (1.8)$$

All models describing coarsening are much less advanced than those describing microsegregation. Only the easiest geometries are treated and no model takes into account a possible interaction between coarsening and segregation [40]. Articles that model segregation either neglect coarsening completely or consider only very simple models (e.g. a phenomenological linear coarsening model in [34] or an Ostwald type model in [33]).

### 1.2.3. Homogenisation during Heat Treatment

Some experimental results concerning the homogenisation of banded microstructures were given in section 1.1.2. The modelling of homogenisation was reviewed by Purdy and Kirkaldy [44] and Martin and Doherty [39]. Any given concentration profile can be represented by a Fourier

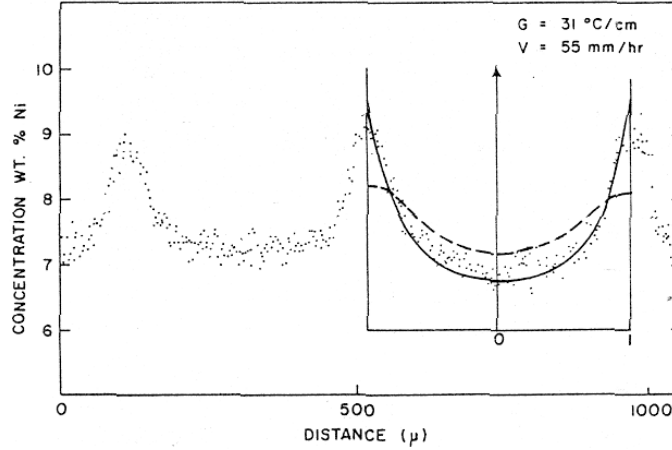


Figure 1.6.: Concentration profile of a Fe-8wt.-% Ni alloy. The approximate profile after annealing at 1220°C for 72 h is shown by the broken line. [44]

series. This series is then used to solve Fick's second law. In a first approximation, the original concentration profile (at  $t = 0$ ) is given by

$$C(x, 0) = C_0 + \Delta C \cos \frac{2\pi x}{\lambda}, \quad (1.9)$$

where  $C_0$  is the average concentration,  $\lambda$  the wavelength,  $\Delta C$  the amplitude of the concentration profile and  $x$  the distance co-ordinate. Fick's second law can be solved analytically. The concentration profile after homogenisation is

$$C(x, t) = \Delta C + p_4 \cos \frac{2\pi x}{\lambda} \exp\left(-\frac{D_S \pi^2 t}{4\lambda^2}\right). \quad (1.10)$$

It is worth noting that the relaxation time is strongly dependent on the segregation wavelength. Therefore, sharp spikes in the concentration profile will vanish rapidly upon homogenisation. Figure 1.6 reflects this behaviour.

For multicomponent systems, the concentration profile of each component can be presented as a Fourier series. The corresponding diffusion equations can be solved using finite-difference methods if the interdiffusion coefficients of the alloying elements are known. The influence of one solute on the diffusion of another can be pronounced [44].

An analysis similar to the one described here was employed by van der Zwaag and co-workers to study the homogenisation behaviour of different steels [45, 46]. They used a second order polynomial as concentration profile ("for mathematical convenience") and found reasonable agreement with experiments by Grange [19] and Offermann et al. [47].

#### 1.2.4. Effect of Deformation on Segregation Profiles

There are only few publications regarding the changes that the microsegregation profile undergo during plastic deformation. Most researchers are either concerned with the development of microsegregation models or model the phase transformation assuming a certain profile.

Verhoeven [4] notes this absence of publications and speculates that the banding planes are exactly parallel to the deformation plane because planes of isoconcentration (e.g. all interdendritic regions) might become aligned during the plastic deformation process. Martin and Doherty [39] consider a simple cubic array of dendrites that is deformed by an extrusion process that reduces the diameter of an ingot by the factor  $1/R$ . Along certain crystallographic directions, the dendrites are then closer packed by a factor  $1/R$ , while along others, the spacing increased by  $R^2$ . This simple model could be applied to segregation profiles by multiplying their amplitude with the appropriate factor depending on orientation.

It also possible to simulate the evolution of a microstructure during deformation by means of crystal plasticity models or by finite element analysis, but the assessment of such models is beyond the scope of this survey.

### 1.2.5. Phase Transformations in Segregated Microstructures

In the previous sections, models were presented that can predict the shape and wavelength of microsegregation profiles. The question as to whether a banded microstructure will evolve upon cooling of such a material will be addressed in this section.

Offermann et al. [47] used a phenomenological approach to predict banding in isothermally heat treated steel. They observed that the degree of banding decreased with decreasing annealing temperature. Concentration profiles obtained by electron probe microanalysis were used to calculate the difference of local  $A_{r3}$  temperature in the microstructure due to segregation using a thermodynamical database (see figure 1.7). From experimental data, two criteria were determined that have to be fulfilled for banding to occur. Firstly, the rate of nucleation of ferrite in the region of increased  $A_{r3}$  temperature must be more than 6-8% larger than the rate in the regions with normal  $A_{r3}$  temperature. The rate of nucleation was calculated using classical nucleation theory. Secondly, the annealing temperature must be high enough that carbon can diffuse over one half of the segregation wavelength during the duration of the heat treatment. These criteria were successfully employed by Rivera-Díaz-del Castillo et al. [45]. Offermann et al. also cite a similar study for continuously cooled steel by Grossterlinden et al. [48] that predicts a critical cooling rate for band formation.

Bhadeshia [49] calculated the volume fraction of ferrite in a banded microstructure. In a homogeneous material, the amount of ferrite and pearlite can be determined from the phase diagram by the lever rule. This does not hold for materials with varying concentrations. Instead, it is assumed that ferrite grows until the carbon concentration in austenite  $C_\gamma$  is as high as the concentration  $C_\gamma^{\text{pe}}$  determined by the paraequilibrium phase diagram. The concentration of carbon in austenite increases during ferrite growth because carbon is rejected from forming ferrite. It is therefore a function of the fraction ferrite  $f_F$  and can be written as

$$C_\gamma = \frac{C_0 - f_F C_\alpha^{\text{pe}}}{1 - f_F} \quad (1.11)$$

where  $C_0$  denominates the average concentration of carbon in the material and  $C_\alpha^{\text{pe}}$  the carbon concentration in ferrite at the ferrite/pearlite interface. To determine  $C_\gamma^{\text{pe}}$  and  $C_\alpha^{\text{pe}}$ , the ternary phase diagram Fe-C-X (with X being the segregated element) must be known. Both concentrations are dependent on the concentration of the alloying element  $C_X$  and, because a concentration profile exists for this element, also on the fraction ferrite  $f_F$ . To obtain this dependence of the paraequilibrium concentrations, the segregation profile  $C_X(f_F)$  need be known. Bhadeshia assumed a triangular profile, but in principle every other profile could be used. As long as the band

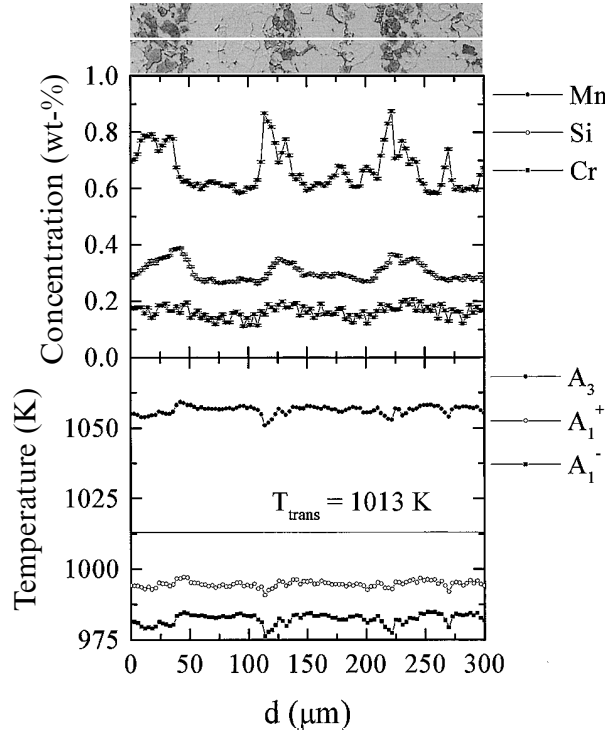


Figure 1.7.: Concentration profiles measured by EPMA, the corresponding (banded) microstructure and the calculated local  $A_{r3}$  temperature [47]

width is not of interest, the wavelength of the segregation profile must not be known to calculate the maximum fraction ferrite. If it is known, however, the band width can be calculated with this method. The proposed calculation assumes paraequilibrium, i.e. the diffusivity of the alloying element X is negligible, and an infinitely fast diffusion of carbon. The whole line of argument is therefore purely thermodynamic. It is not unlikely that the assumption of infinitely fast carbon diffusion holds for continuous cooling or even relatively fast isothermal reactions. Additionally, the microstructure of the material is neglected. There are cases in which ferrite formation is limited by the number of available nucleation sites (see section 1.1.2).

Another approach to model phase transformation behaviour are kinetic models. Starting with the works of Johnson and Mehl [50] and Avrami [51], the kinetic theory of phase transformations has been developed in great detail. For a recent review of solid state transformation kinetics models see [52]. If the final volume fractions of all possible phases in steels are to be predicted correctly, a model must be used that allows for the simultaneous transformation of austenite to all these phases. A model taking into account allotriomorphic ferrite, Widmanstätten ferrite and pearlite was published by Jones and Bhadeshia [53]. Kinetic models don't explicitly include microstructure, but certain choices about the microstructure must be made before applying the models. For example, the kinetics of phase transformation is different if nucleation starts at grain boundaries than if it starts inside grains. Likewise, the model in [53] adopts certain nucleation modes, shapes, aspect ratios and growth modes for all phases that have been determined experimentally. This is described in more detail in section 2.1. With these adoptions and with the volume fractions of all phases after transformation, key features of the microstructure are given.

The aim of this work was to include a microsegregation profile in a kinetic model in order to investigate the resulting microstructure after phase transformation. Of major interest is the question whether banding can be correctly predicted from such calculations.

# Chapter 2.

## The Method

### 2.1. The Model

Classical Johnson-Mehl-Avrami theory describes the transformation of a single phase to one product phase. In steels, austenite can transform upon cooling into several different phases such as allotriomorphic ferrite, Widmanstätten ferrite, bainite, pearlite and martensite. These phases will often form simultaneously, following different transformation mechanisms. Therefore, a kinetic model for phase transformation in steel must allow for simultaneous phase transformations and must describe the transformation mechanisms of the different phases as accurate as possible. The former is achieved by numerically solving all (coupled) impingement equations simultaneously, the latter by choosing the appropriate expressions for nucleation and growth. The formalism of simultaneous phase transformations was described by Robson and Bhadeshia [54] and Jones and Bhadeshia [53]. All equations below are taken from these references. Details for the decomposition of austenite to ferrite and pearlite can be found in [53, 55].

Nucleation and growth equations assume that there is unlimited space into which the phase can grow (the “extended space”). Therefore, the transformed volume of phase  $j$  given by these equations is not the true volume  $V_j$ , but the “extended volume”  $V_j^e$ . To calculate the true transformed volume from the extended volume, one must take into account impingement, which means a correction for the fact that nucleation cannot take place in regions that are already transformed and that phases cannot grow into these regions. To obtain the transformed volume, the extended volume is therefore multiplied with the untransformed volume fraction. For a single phase  $\sigma$ , the change in true volume  $dV$  is given by

$$dV_\sigma = \left(1 - \frac{V_\sigma}{V_{\text{tot}}}\right) dV_\sigma^e. \quad (2.1)$$

If the original phase transforms simultaneously into several phases  $j$ , the above equation has to be extended to

$$dV_j = \left(1 - \frac{\sum_j V_j}{V_{\text{tot}}}\right) dV_j^e. \quad (2.2)$$

The extended volume can be calculated for each phase if the mechanisms of nucleation (the nucleation rate per unit volume  $I$ ) and growth (the growth rate  $G$ ) are known. For growth in all three dimensions, the equation that has to be applied is

$$V_j^e = gV_{\text{tot}} \int_0^t G^3 I(t - \tau)^3 d\tau, \quad (2.3)$$

where  $\tau$  stands for the time at which a particle nucleates (its incubation time) and  $g$  is a geometric factor equal to  $4/3\pi$  for a spherical particle. This equation can be integrated if a constant

nucleation rate is assumed and together with equation 2.1 leads to the well known Johnson-Mehl-Avrami equation.

The model in [53] treats nucleation at grain boundaries and inclusions, although the latter were not present in any calculation in this thesis. Phases considered are allotriomorphic ferrite, Widmanstätten ferrite and pearlite. The phases grow both in the grain boundary and into the grain (perpendicular to the grain boundary). In extended space, the grain boundary is a flat plane and the grain a series of planes parallel to the grain boundary with a distance  $\Delta y$  between two planes. Because all nucleation takes place at the grain boundary and particles grow along the boundary, the impingement equation 2.2 must be applied to the extended area  $O_{j,y}^e$ , not only in the grain boundary ( $y = 0$ ), but in all planes. When finite area steps ( $\Delta O$ ) are used instead of infinitely small volume steps ( $dV$ ), equation 2.2 becomes

$$\Delta O_{j,y} = \left(1 - \frac{\sum_j^3 O_{j,y}}{O_B}\right) \Delta O_{j,y}^e, \quad (2.4)$$

where the subscript  $y$  denotes the distance of the plane to the grain boundary,  $O_B$  is the total grain boundary area per unit volume,  $O_{j,y}$  the transformed area and  $\Delta O_{j,y}^e$  the extended area of phase  $j$  on plane  $y$  that is transformed in the period between  $t$  and  $t + \Delta t$ . This equation treats impingement in planes, correcting for nucleation in and growth into areas that are already transformed. Growth perpendicular to the grain boundary would be unhindered in this model and the true volume could be calculated simply by

$$\Delta V_j = \Delta y \sum_{y=0}^{y_{\max}} \Delta O_{j,y}. \quad (2.5)$$

If the equations above were used, the grain boundary would assumed to be flat. For a realistic calculation, an additional impingement equation for the volume has to be used. Therefore, the result of equation 2.5 is  $V_j^e$  and the true volume change in one time step is calculated by

$$\Delta V_j = \left(1 - \frac{\sum_{j=1}^3 V_j}{V_{\text{tot}}}\right) \left(\Delta y \sum_{y=0}^{y_{\max}} \Delta O_{j,y}\right) \quad (2.6)$$

for the three phases considered in the model.

The extended area can be calculated when models for nucleation and growth are assumed. Using finite steps, the integral in equation 2.3 becomes a sum over all  $n_t$  time steps so that  $t = n_t \Delta t$ .

$$\Delta O_{j,y}^e = O_B \sum_{l=0}^{n_t} A_{j,y,l} \Delta t I_{j,l} \Delta \tau \quad (2.7)$$

Here,  $A_{j,y,l}$  is the area growth rate for a particle of phase  $j$  nucleated at time  $\tau = l \Delta \tau$  on plane  $y$  and  $I_{j,l}$  the nucleation rate per unit area at this time for phase  $j$ . In other words, the growth of all particles nucleated between  $t = 0$  and the current time is calculated by multiplying their number (given by the nucleation rate at the time of their nucleation) with their growth rate at the current plane. This growth rate is not a continuous function of  $y$ , but only three cases are considered. Detailed information on the nucleation and growth models can be found in [53]. A summary of the most important assumptions and parameters is presented in table 2.1.

It must be noted that some empirical equations used to calculate nucleation and growth of

Table 2.1.: Assumptions made and constants used for the calculation of nucleation and growth of allotriomorphic ferrite, Widmanstätten ferrite and pearlite [53].

General assumptions	paraequilibrium, random nucleation, three dimensional growth		
Assumptions for:	allotriomorphic ferrite	Widmanstätten ferrite	pearlite
Nucleation	heterogeneous at GB	displacive	heterogeneous at GB
Growth mode	diffusion controlled	interface controlled	interface controlled
Shape	discs <sup>a</sup>	tetragonal prisms	discs <sup>a</sup>
Aspect ratio	3.0	0.02	1.0
References	[56–58]	[59–61]	[62, 63]

<sup>a</sup>parallel to grain boundary

pearlite in the subroutine PEARL are only valid for temperatures above 500°C. Extrapolation below this temperature is possible, but may lead to results that don't agree with experimental evidence. In the model from [53] that is presented here, only three phases are considered. Other phases like bainite can be included in the model as long as nucleation and growth models are known. Martensite formation is only considered by calculating the martensite start temperature. Austenite that is not transformed when the martensite start temperature is reached is assumed to completely transform into martensite.

## 2.2. Modifications to the Original Program

This work is based on the program STRUCTURE that was developed by Jones and Bhadeshia [64]. It is an implementation of the kinetic theory described above in the FORTRAN programming language. A schematic flowchart representation of the program is given in figure 2.1(a). The major modifications made to incorporate a concentration fluctuation into the program are indicated in figure 2.1(b). In the current program, this fluctuation affects the concentration of only one alloying element, but it would be easy to include more elements. Manganese was chosen as affected element because the influence of manganese on banding is well known. The manganese concentration profile is divided into  $n$  discrete steps, each of which is called a “concentration slice”, or short, a slice. Inside the main loop that advances time and temperature steps, another loop was inserted. This “slice loop” repeats all calculations at the current time step for each slice. All calculations that are necessary for each time and slice step were moved to a subroutine “STRUCTURE”. The values of all relevant variables for each slice are stored outside the loops and are passed on to the subroutine STRUCTURE. These variables include the volume fractions of all phases, the number of nuclei at the previous time step and all other variables that are updated (as opposed to recalculated) at the current time step. Because the manganese concentration changes between iterations of the slice loop, the phase diagram and all driving forces have to be recalculated at each slice and time step, not only once as in the original program. The calculation of the carbon concentration in remaining, untransformed austenite, however, must take place outside the slice loop (but inside the time loop).

The calculation of the carbon concentration in untransformed austenite is the only point in the program where the slices interact with each other. In the original program, the carbon enrichment is calculated in the following way: The amount of carbon in growing allotriomorphic and Wid-

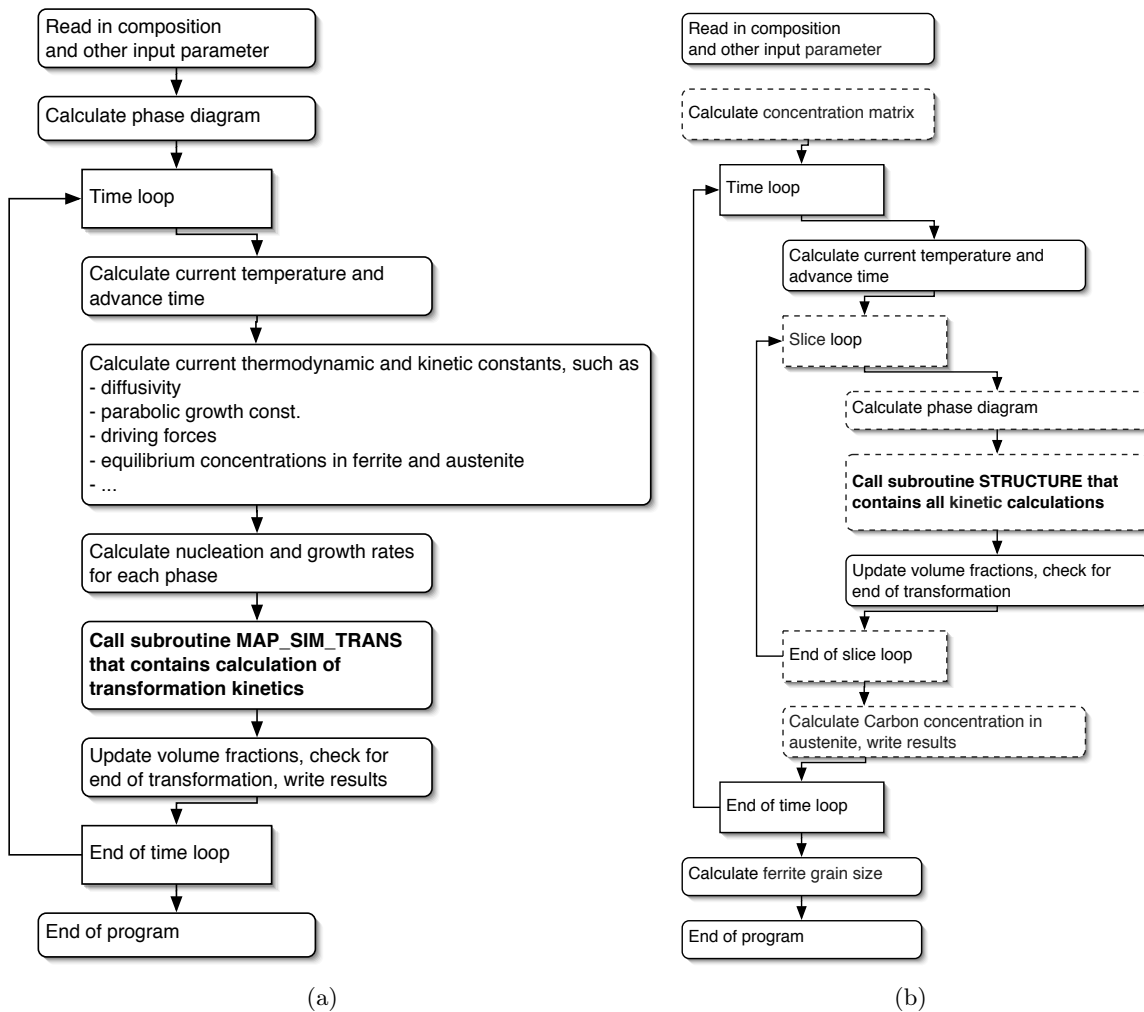


Figure 2.1.: Flowchart representations of the original program (a) and major additions to it (b). New or moved program parts are circled with dashed lines.

manstätten ferrite (growing pearlite does not reject carbon because of cementite precipitation) is determined by multiplying the transformed fraction of these phases with the carbon concentration in ferrite that is in equilibrium with austenite,  $C_\gamma^*$ . If this is subtracted from the average carbon concentration in the sample,  $C_0$ , the amount of carbon rejected from growing ferrite is known. This amount is divided by the untransformed volume fraction to yield the concentration of carbon in untransformed austenite.

$$C_\gamma = \frac{C_0 - (C_\alpha^* (f_{AF} + f_{WF}))}{1 - (f_{AF} + f_{WF})} \quad (2.8)$$

In the modified program, the *average* phase fractions of ferrite and pearlite in all  $n$  slices are used and therefore the transformed fractions of all slices are summed. This is the same as assuming that carbon can partition between slices with an infinite velocity. At the same time, partitioning of other elements between slices is completely neglected and thus paraequilibrium conditions are simulated.

$$C_\gamma = \frac{C_0 - \frac{1}{n} \sum_{k=1}^n (C_{\alpha,k}^* (f_{AF,k} + f_{WF,k}))}{1 - \frac{1}{n} \sum_{k=1}^n (f_{AF,k} + f_{WF,k})} \quad (2.9)$$

As mentioned before, this is the only place in the program where the slices interact. Apart from this calculation of carbon enrichment, the slices are treated as completely independent entities. The program is therefore still a continuum calculation: there was no notion of length introduced and therefore no concentration fluctuation “wavelength”.<sup>1</sup> If however a finite diffusivity of carbon was assumed, a length scale would have to be introduced. During one time step, carbon can only diffuse a certain distance that can be estimated by Fick’s first law if the carbon concentration in each slice and the concentration fluctuation wavelength (= the average diffusion distance) is known. Because the concentration fluctuation wave length is not treated in the current model, the response of the model becomes unrealistic at high cooling rates where the assumption of infinitely fast carbon partitioning is not justifiable.

There are two pieces of information regarding the microstructure of the material in the program. One is the austenite grain size which determines the grain boundary area available for nucleation, the other is the assumption, that nucleation only takes place at grain boundaries. The density of nuclei is assumed to be homogeneous. If a concentration fluctuation wavelength was introduced in the program as it is, it would only mean that a part of the available nucleation sites would lie in regions of high manganese concentration and the rest in regions of low Mn-concentration, effectively lowering the nuclei density for each region. This is exactly the effect that the austenite grain size has. The two parameters would therefore act in the same way and it would make no sense to vary them independently. A large grain size with a large concentration wavelength would produce exactly the same result as a small grain size with a small concentration wavelength.

This reasoning is true even if the model would make use of a length scale. In the case when the concentration wavelength is small compared with the austenite grain size, the grain boundary of one grain “sees” all different concentrations. Even if the concentration wavelength would be in the same order of magnitude than the grain size so that one grain boundary would “see” only a certain concentration, the average over all grain boundaries would still be the same as in the case of a small wavelength.

<sup>1</sup>Austenite grain size is input as a length, but is immediately converted into an area per unit volume by a geometric equation.

In reality, concentration fluctuation amplitude and wavelength will often be connected. A higher cooling rate during solidification will lead to a finer microstructure (i.e. a smaller fluctuation wavelength). At the same time, the concentration  $C_S$  (cf. figure 1.5(a)) of the first crystallites to form will also be higher, and thus the amount of alloying element that is rejected lower. This leads to a smaller concentration fluctuation amplitude. Strictly speaking, it is therefore impossible to separate the two effects.

The subroutine PEARL that calculates the growth of pearlite can only treat ternary systems. It is therefore modified to use the manganese concentration in all calculations in order to capture effects caused by fluctuating manganese concentration. As mentioned in the previous section, empirical equations in this subroutine become unreliable below 500°C where they may predict pearlite growth even if this is extremely slow in reality. Calculations are therefore stopped at this temperature regardless whether there is still untransformed austenite left or not. It should be considered to improve PEARL so that this artificial abortion of the simulation to reproduce experimental data becomes unnecessary. Equally, the calculations are stopped if the transformed fraction exceeds 99%. If this threshold is only reached in one slice, transformation in the other slice(s) continues until the overall transformed fraction reaches 99% (or the temperature drops below 500°C).

## 2.3. Input Parameters

### 2.3.1. Constants

A typical input file for a calculation is included in Appendix B. It includes a number of input parameters, some of which are kept constant during all calculations. These constants, whose values were taken unmodified from Jones and Bhadeshia [53], are:

**Austenite-ferrite interfacial energy** This is the interfacial energy between austenite and allotriomorphic ferrite. Its value is 0.022 J/m<sup>2</sup>. It is used in the calculation of the nucleation and growth rate of allotriomorphic ferrite.

**Activation energy for atomic transfer** Together with the interfacial energy, this forms the activation energy for the atomic transfer across a moving interface. Its value is determined to be 200 kJ/mol by fitting the model to experimental data [55].

**Aspect ration for the nucleation of ferrite** This determines the aspect ratio of allotriomorphic ferrite nuclei at grain boundaries. Its value is 0.333, corresponding to an aspect ratio of 3 for the growth of allotriomorphic ferrite.

**Fraction of effective boundary sites** This is the pre-exponential factor for nucleation of allotriomorphic ferrite at the grain boundary. It is set to 10<sup>-8</sup>.

**Total volume fractions of inclusions** This parameter is set to zero, which means that there are no inclusions present. The values of the parameters fraction of effective inclusions, shape factor for nucleation on an inclusion and mean inclusion diameter are therefore irrelevant.

**Nucleation factor for pearlite** This is the pre-exponential factor for nucleation of pearlite at the grain boundary. It is set to 10<sup>-5</sup>.

**Aspect ratios of growing allotriomorphic ferrite, Widmanstätten ferrite and pearlite** These aspect ratios are set to 3, 0.05 and 1, respectively. This means that for example nuclei of

allotriomorphic ferrite will grow three times faster in a direction parallel to the grain boundary than perpendicular to it. Details can be found in [53].

### 2.3.2. “Technical” Parameters

This section describes input parameters that don’t have a physical meaning. Nevertheless, some of them influence the result of the calculations and their value must therefore be set carefully. Others don’t control the result, but the speed of the calculations. First, an overview is given before the most important parameter are described in detail.

**Type of heat treatment** All calculations are conducted starting at a high temperature in the austenite phase field with subsequent cooling at a constant cooling rate.

**Maximum number of iterations** This number determines the maximum number of times the main loop in the program is executed. It is set to 50,000, but this many cycles are never actually needed. One of the exit criteria (e.g. finished transformation or temperature drops below 500 °C) always becomes true before 50,000 is reached.

**Analytical comparison** Set to zero, meaning that there are no analytical models calculated for comparison with the results of the numerical calculation.

**Maximum number of planes** This parameter determines the maximum number of planes used in the calculation of the progress of the transformation in extended space. Similar to the maximum number of iterations, it has no physical meaning, but it must be kept large enough. For most combinations of input parameters, a value of 15,000 ensures this.

**Time step** This parameter had to be determined for each individual calculation to ensure numerical accuracy.

**Number of slices** A slice is a region of homogeneous composition. Most, but not all calculations were performed with two slices.

**Concentration fluctuation profile shape** This is the function that is used to calculate the manganese concentration in the slices. In all but one calculation, a sinusoidal concentration profile shape is used. In one calculation, a Scheil-type equation is applied.

The value of the **time step** can have a considerable influence on the results of calculations. See table 2.2 for a comparison of volume fractions of all three phases after transformation and of the number of iterations needed for the simulation. In these calculations, the “standard” set of input parameters was used and the only parameter that was varied was the time step. For an explanation of this set of input parameters see section 2.3.3. It is obvious that a smaller time step increases the run time of the program, so a larger time step is desirable. Too large a time step, on the other hand, changes the result of the calculation. This can also be seen in figure 2.2, where the total volume transformed is plotted versus the temperature. The curve for the calculation with a time step of 10 s is at higher temperatures than the curves for smaller time steps. It also ends at a lower value of the total transformed volume. This is due to the fact that the program stops as soon as the next time step would take the total transformed volume fraction to a value larger than 0.99 (in this case, it would probably take it to a value above 1.0, which is physically meaningless). It is clear that there are not enough points on this curve to draw a continuous line. The curves for time steps 0.5 s and 0.1 s, however, contain so many data points that they were

Table 2.2.: Volume fractions of all different phases after complete transformation for different time steps as well as the number of calculation cycles needed for the simulation. Calculations with “standard” set of input parameters.

time step / s	number of cycles	allotriomorphic ferrite	Widmanstätten ferrite	pearlite
10.0	20	0.485	0.195	0.195
5.0	43	0.475	0.195	0.310
2.5	90	0.460	0.210	0.320
1.0	229	0.450	0.220	0.325
0.5	462	0.440	0.225	0.320

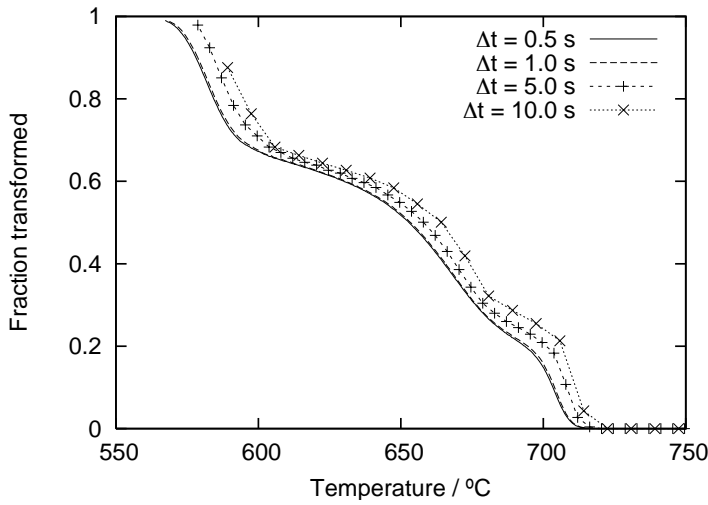


Figure 2.2.: Total transformed volume fraction versus temperature for different time steps.

omitted for better legibility of the graph. The two curves are almost identical and also the phase fractions in table 2.2 are very similar. It is therefore unnecessary to reduce the time step further. In this case, a calculation with a time step of 1.0 s shows the optimal balance between accuracy and calculation speed. For each problem in this thesis, a series of calculations was performed to ensure that the time step is low enough. The time step that was finally chosen is not mentioned in each case.

It is also worth noting that table 2.2 can give an indication about the accuracy of calculations: Even though a small time step is chosen, the phase fractions differ at the second decimal place. An error of at least 2 to 3 % seems to be usual in these calculations.

The shape of the **concentration fluctuation profile** is technically not an input parameter, because it cannot be specified in the input file. It must be changed in the source code of the program by modifying the subroutine `CONCPROFILESHAPE` that takes as input the average manganese concentration and fluctuation amplitude as well as the number of slices and returns the manganese concentration in each slice. To calculate the Mn-concentration in each slice, a function is evaluated at a number of points equal to the number of slices. These points are distributed evenly over one half of the wavelength of the fluctuation (which has, as mentioned before, no

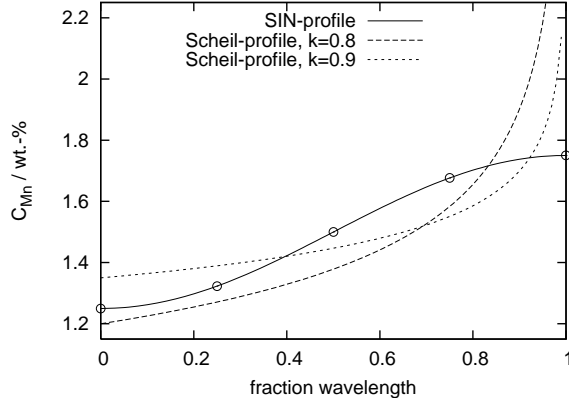


Figure 2.3.: The used concentration profiles. SIN-profile refers to equation 2.10 and Scheil profile to equation 2.11.

physical meaning in the current program and is therefore set to 1). In most calculations, this function is a sinusoidal one ( $C_{\text{Mn}}^1(x)$ ). To assess the influence of the concentration fluctuation shape, additional calculations with Scheil-type profiles ( $C_{\text{Mn}}^2(x)$ , see section 1.2.1) and two different values for the partition coefficient  $k$  were performed. Both functions are shown in figure 2.3 as lines. As an example, the concentrations of five slices calculated using the sinusoidal function are drawn as points in the figure. The functions are given by

$$C_{\text{Mn}}^1(x) = C_{0,\text{Mn}} - \Delta C_{\text{Mn}} \cos\left(\frac{x-1}{n}\pi\right) \quad (2.10)$$

$$C_{\text{Mn}}^2(x) = C_{0,\text{Mn}} k \left(1 - \frac{x-1}{n}\right)^{k-1}. \quad (2.11)$$

The values of  $k$  were chosen to lead to a similar maximum and minimum manganese concentration in the first and last slice as the sinusoidal function. The total amount of manganese in the sample can be calculated by integrating equations 2.10 and 2.11 from  $x = 1$  to  $n$ . It is larger when the sinusoidal function is used than when the Scheil equation is used, but using higher values for  $k$  would lead to unrealistically high maximum Mn concentrations.

The results of the calculations with different concentration profile shapes are shown in figure 2.4. The transformed fractions of all phases after complete transformation are plotted versus the manganese concentrations in the slices. The simulations were done using the “standard” set of input parameters and a total slice number of  $n = 20$ . The average manganese concentration  $C_{0,\text{Mn}}$  in all cases was 1.5 wt.-%. For the lower value of  $k$  where the maximum and minimum manganese concentrations are similar to the sinusoidal function, the transformed fractions are very similar for both functions. The shape of the concentration profile seems to have only a minor influence on the result of the calculations (if all parameters were chosen carefully). The sinusoidal profile is used in all further simulations because the fluctuation amplitude can be varied in an easy way.

The **number of slices** is another important parameter that determines the result of simulations. If it equals one, the behaviour of the original program is recovered. If it equals two, an arrangement of two alloys of different Mn content that are closely attached to each other is simulated, similar to the one used in [1]. If several slices are used, a material with a composition

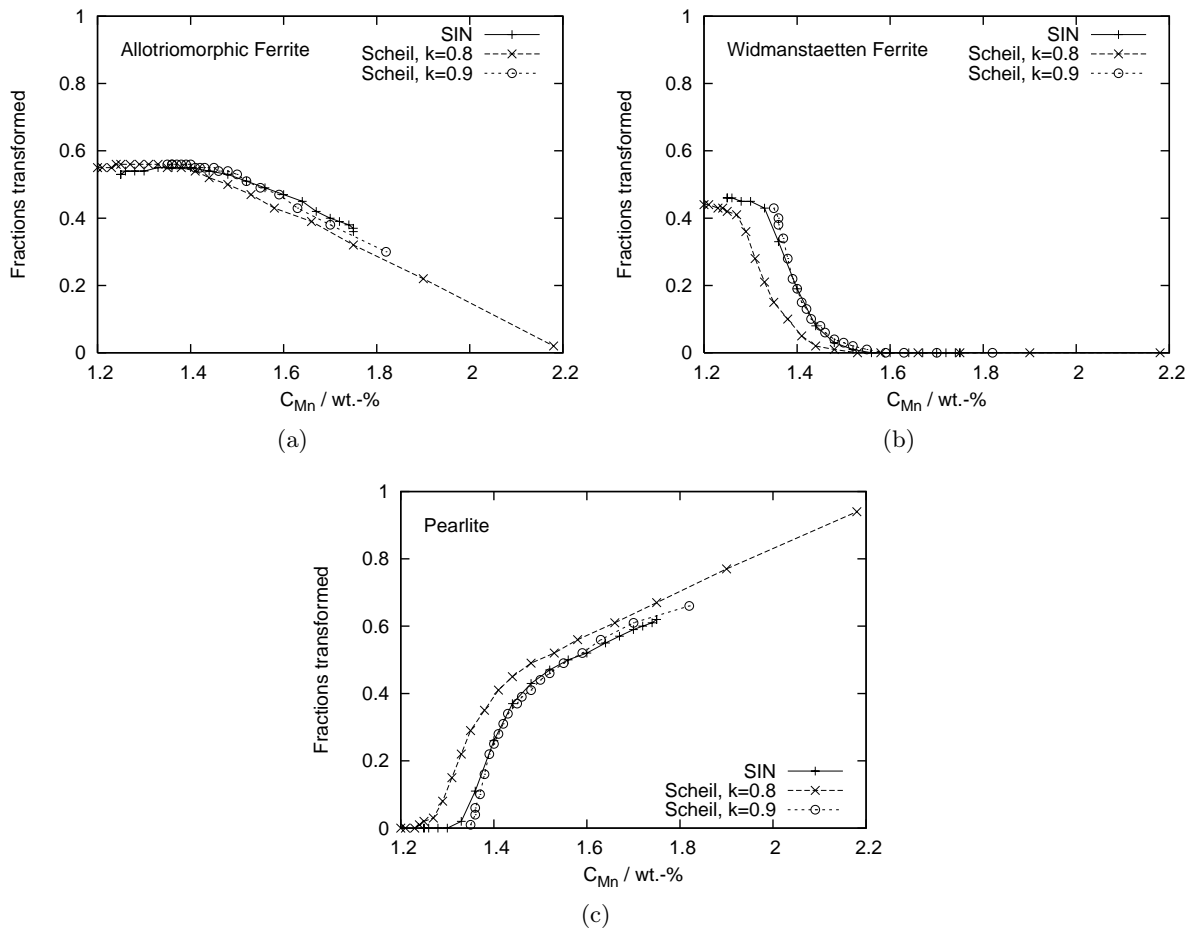


Figure 2.4.: Volume fractions of the different phases after transformation as a function of the manganese concentration in the slices. Calculations were done for the “standard” set of input parameters and 20 slices. SIN and Scheil refer to equations 2.10 and 2.11, respectively.

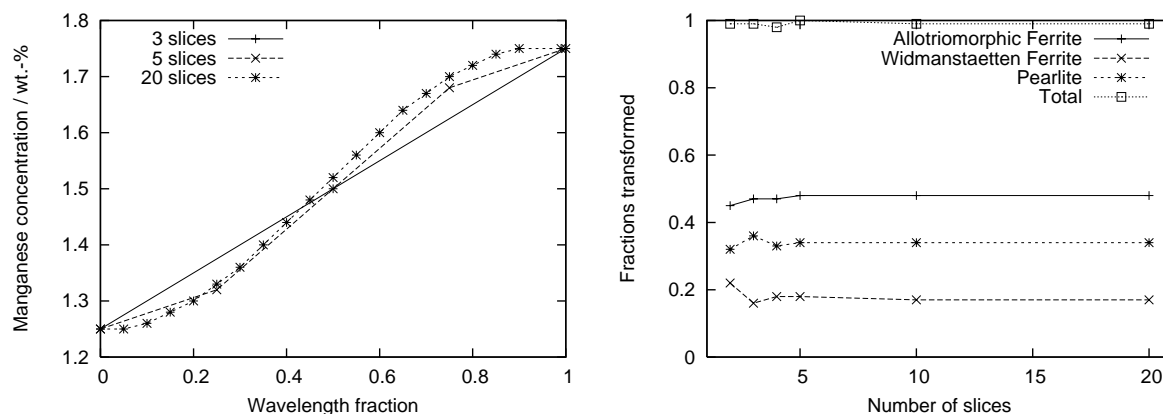


Figure 2.5.: (a) Manganese concentrations as a function of slice number for different numbers of slices. The slice numbers have been normalised with the total slice number. (b) Transformed volume fractions of all different phases versus the number of slices used in the calculations. The “standard” set of input parameters was used with the same average manganese concentration and the same concentration fluctuation amplitude.

profile is simulated. The number of slices then determines how coarse or fine the discretisation of the composition profile is. Figure 2.5(a) shows the Mn-concentrations in the slices depending on the number of slices, and Figure 2.5(b) shows the average volume fractions of all phases in all slices after complete transformation as a function of the number of slices used in the calculation. All other input parameters were taken from the “standard” set and the concentration fluctuation profile is a sine function. The results vary for calculations with two, three or four slices while they are approximately the same for calculations with five, ten or 20 slices. A concentration profile with five slices is still quite coarse, but it is apparently fine enough when only the total transformed fractions are of interest. Figure 2.6 shows more details. In these three graphs, the volume fractions of all phases are plotted versus the manganese concentration in the slices for different numbers of slices. It can be seen that the calculation with five slices produces a curve very similar to the one with twenty slices. Again, no additional information is gained when the slice number is larger than five.

An interesting feature of these graphs is their S-shape. This can be clearly seen when the fraction of pearlite is plotted versus the wavelength fraction (figure 2.6(d)). Between 0.25 and 0.45 of the wavelength, there is a narrow region where the fraction of pearlite increases rapidly. But even if the transformed fractions are plotted versus the concentration, there is a region in which the phase fraction of pearlite varies rapidly (approx. between 1.3 and 1.5 wt.-% manganese) and other regions in which the fraction varies only slowly (above 1.5 wt.-% Mn). This sharp increase in the fraction of pearlite could in principle be used to define the width of a pearlite band.

For most of the calculations in this thesis, a slice number of two was selected. Even if a system comprising two slices is only a first approximation of a real system with banding, it captures the essential features (one region with high and one region with low Mn-content) and produces results that are simple to visualise and interpret.

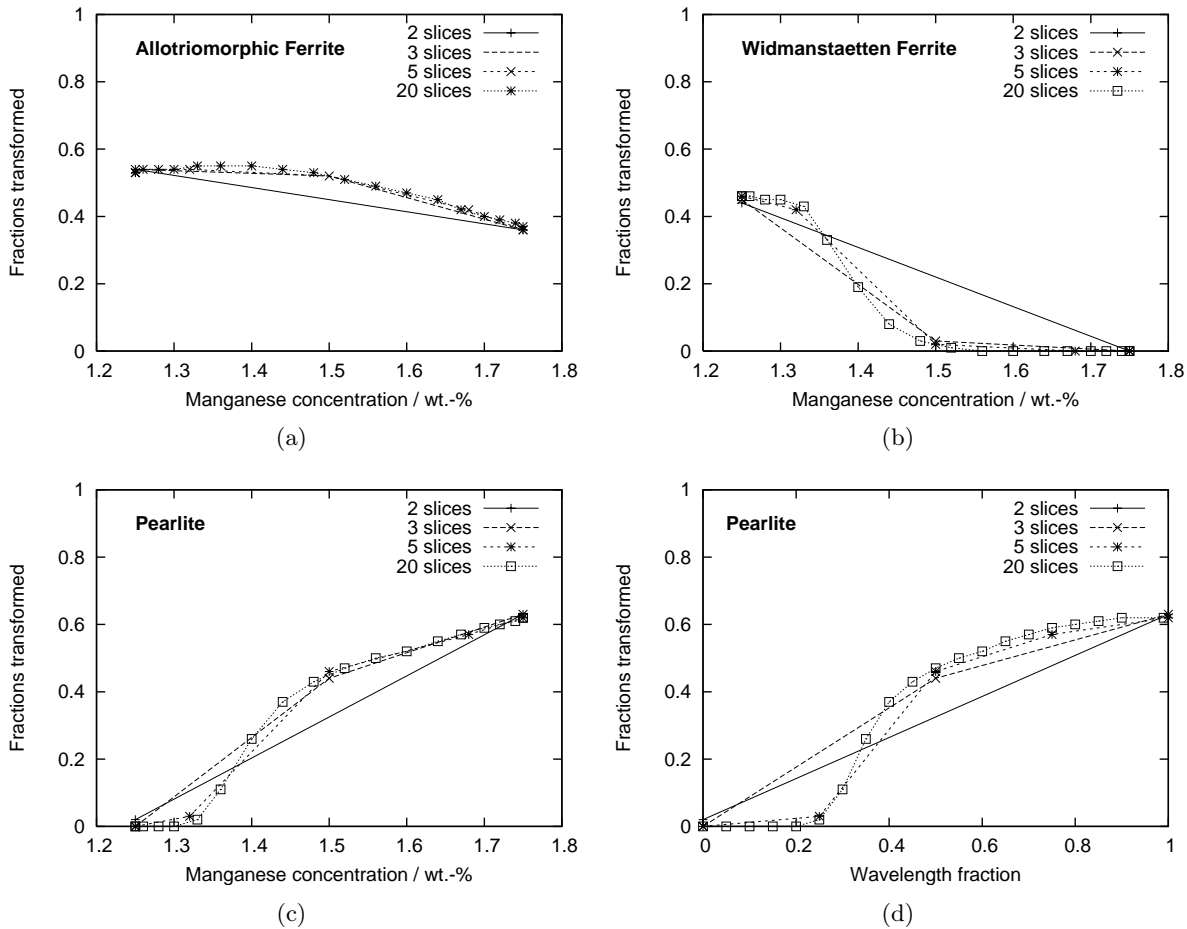


Figure 2.6.: Volume fraction of the different phases versus the manganese concentration for calculations with different numbers of slices. In (d), the fraction of pearlite is plotted versus the wavelength fraction instead of the Mn-concentration.

### 2.3.3. Varied Parameters

The parameters that were studied are listed below. The results for each series of calculations are displayed and discussed in chapter 3.

**Composition** The program can take into account the concentrations of carbon, silicon, manganese, nickel, molybdenum, chromium and vanadium. While most parts of the program (for instance the calculation of the thermodynamic driving forces) actually consider all alloying elements, the subroutine that calculates pearlite growth is only written for a ternary system. The system Fe-C-Mn is passed on when this subroutine is called. It is also important to know that the calculation of the interlamellar spacing of pearlite and its critical value in the subroutine PEARL is based on an empirical expression that is only strictly valid for manganese concentrations up to 1.8 wt.-% manganese [63]. Calculations with a higher Mn concentration contain unjustified extrapolations of these equations and could therefore lead to erroneous results for the growth of pearlite.

Table 2.3.: Input parameters of the tree different sets. Data for set “A” taken from [1], for set “B” from [2]

Parameter	set “standard”	set “A”	set “B”
Composition in wt.-%			
carbon	0.2	0.202	0.15
silicon	0.2	0.027	0.2
manganese	1.5	1.65	1.9
nickel	0.0	0.0	0.0
molybdenum	0.0	0.0	0.0
chromium	0.0	0.034	0.2
vanadium	0.0	0.0	0.0
Austenite grain size	20 $\mu\text{m}^*$	20 $\mu\text{m}^\dagger$	20 $\mu\text{m}^\dagger$
Cooling rate	50 $\text{K min}^{-1}^*$	varied	varied
Mn fluctuation amplitude	$\pm 0.25 \text{ wt.-%}^*$	$\pm 1.65 \text{ wt.-%}$	$\pm 0.25 \text{ wt.-%}^\dagger$

\* These parameters were varied. The given values are the standard ones when they were kept constant and other parameters were varied.

† These parameters were not given in the literature.

Three different compositions were studied. Details are given in table 2.3.

**Cooling rate** The cooling rate is an important parameter, because above a certain CR, banding should become suppressed (cf. section 1.1.2).

**Austenite grain size** The grain size is read into the program as a mean linear intercept. From this quantity the grain boundary area per unit volume is calculated. Each slice has the same grain boundary area.

**Concentration fluctuation amplitude** This value is added and subtracted from the mean value to give the maximum and minimum Mn concentration. Slice 1 always has the lowest Mn concentration and the last slice (often slice 2) always the highest Mn concentration.

To test the program, all parameters mentioned above were varied systematically in a common system showing banding. The set of parameters used in this calculations is referred to as the “standard” set of parameters. Apart from the composition, all values were determined in preliminary calculations so that banding is most clearly visible. The used parameters are summarised in table 2.3 and the results of these calculations are presented in section 3.1. Subsequently, it was attempted to reproduce the experimental results given by Kirkaldy et al. [1] and Caballero et al. [2]. For this purpose, data sets were used that are as similar as possible to the materials used in the literature. If no values for one parameter were given, the same values as in the “standard” set were chosen. The values for these sets of parameters are also compiled in table 2.3.

## 2.4. Output

The standard outputs of the program are the elapsed time, the temperature and transformed fractions of all three phases at each time step as well as the reason why the program stopped

(transformation finished, temperature lower than 500 °C, error message). Additionally, the temperatures and times at which one percent of the total volume is transformed to each phase are recorded to facilitate the plotting of a continuous cooling diagram. A subroutine was written that calculates the approximate average grain size of allotriomorphic ferrite  $D_{AF}$  according to the following equation which was taken from [65].

$$D_{AF} = \left( \frac{2}{3N_{v,AF}} \right)^{\frac{1}{3}} \quad (2.12)$$

Here,  $N_v$  means the total number of allotriomorphic ferrite particles per unit volume. This number can be calculated from the number of ferrite nuclei at each of the planes at which transformation can happen, but it must be taken into account that not each nucleus will be “successful” and lead to a particle: Nucleation cannot take place in already transformed regions. Therefore, an equation analogous to the calculation of the transformed volume from the extended volume is employed. The number of successful nuclei,  $N_{v,AF}$ , is calculated by multiplying the total number of nuclei on one plane  $k$ ,  $N_{AF,k}$  with the untransformed area fraction of this plane and summing over all  $n_k$  planes:

$$N_{v,AF} = \sum_k^{n_k} N_{AF,k} \left( 1 - \frac{\sum_{j=1}^3 O_{j,k}}{O_B} \right) \quad (2.13)$$

The calculation above is only valid if it is assumed that all nuclei are distributed randomly. Also note that these grain sizes are calculated independently for each slice.

## 2.5. Accuracy of Calculations

The accuracy of the performed calculations is difficult to estimate. Of course, care must be taken that the employed time step is small enough as explained in section 2.3.2. If this is guaranteed, there is a remaining small variation between calculations with similar time steps of the order of 2 to 3% in the volume fractions of the different phases. This is due to the fact that the volume fraction of a phase can increase by this much in one time step, so only one additional step in the calculation can lead to this variation. Another factors leading to numerical inaccuracy in the program are the usage of the `REAL` data type instead of the `DOUBLE PRECISION` type in many places in the code. At several places in the program, it is checked whether transformation is complete (e.g. transformation of a particular phase in a particular slice). This check is true if the volume fraction is larger than 0.99, leaving the last per cent disregarded.

The used model includes many details about the transformation behaviour of the different phases. Numerous assumptions and approximations are made and some of the calculations rely on empirical equations. Amongst others, the phase diagram is calculated in the program, diffusivities and thickening constants and empirical values are used for nucleation factors, aspect ratios and activation energies. All these approximations could, in principle, add to the error in the program, however, the equations and parameters have been carefully chosen and validated and the original program `STRUCTURE` has been shown to be able to reproduce experimental results [53].

The most unrealistic assumption and therefore the largest contribution to the inaccuracy of the program is probably the assumption of infinitely fast carbon partitioning in the calculation of the carbon enrichment. The elimination of banding at high cooling rates is known to be due to the finite partitioning of carbon, so a model that fails to include this effect is unlikely to produce accurate results.

# Chapter 3.

## Results and Discussion

### 3.1. The Effect of Various Input Parameters

In this section, calculations conducted with the “standard” set of input parameters are presented. Several input parameters were varied systematically as described in section 2.3.3.

#### 3.1.1. Carbon Partitioning

At first, a “standard” calculation was performed with and without carbon partitioning between the slices to check whether the program is producing a banded microstructure at all. The results are given in figure 3.1 where the accumulated transformed fractions are plotted versus the temperature. For the calculation without carbon partitioning (figure 3.1(a)), both slices show a similar transformation behaviour. At high temperatures, allotriomorphic ferrite is formed, followed by Widmanstätten ferrite and finally pearlite. Slice 1, the slice with a low manganese concentration, transforms into slightly more ferrite than slice 2 and transformation to Widmanstätten ferrite and pearlite happens at higher temperatures, but the final fractions of allotriomorphic ferrite, Widmanstätten ferrite and pearlite are similar. When carbon partitioning is allowed, almost all pearlite forms in the slice with a high manganese concentration (figure 3.1(b), slice 2), while the slice with a low manganese concentration consists almost entirely of ferrite. This is exactly the expected behaviour: Manganese is an austenite stabilising element and so transformation to ferrite takes place in low-Mn regions first, enriching high-Mn regions with carbon which in turn leads to pearlite formation. Figure 3.1 shows that it is possible to simulate banding with the presented computer program.

The visible steps in the run of the curves, for example for allotriomorphic ferrite in the calculation with carbon partitioning are not due to the chosen time step. Reducing the time step does not make the curves smoother because the reason for steps lies in the finite step in the volume fractions which are printed out with a precision of two decimal places.

#### 3.1.2. Cooling Rate

It is known since a long time that banding can be suppressed by high cooling rates (see section 1.1.2). Above a certain critical cooling rate, a homogeneous microstructure is obtained even though the underlying concentration fluctuation persists. To investigate whether this behaviour can be reproduced, the cooling rate of “standard” calculations was varied from  $1 \text{ K min}^{-1}$  to  $1200 \text{ K min}^{-1}$ . The results are displayed in three ways. Figures 3.2 and 3.3 show the accumulated transformed fractions as a function of temperature with one subfigure per slice and per cooling rate. The final transformed fractions of all phases are presented in figure 3.4 as a function of cooling rate. Additionally, a continuous cooling diagram was compiled (figure 3.5).

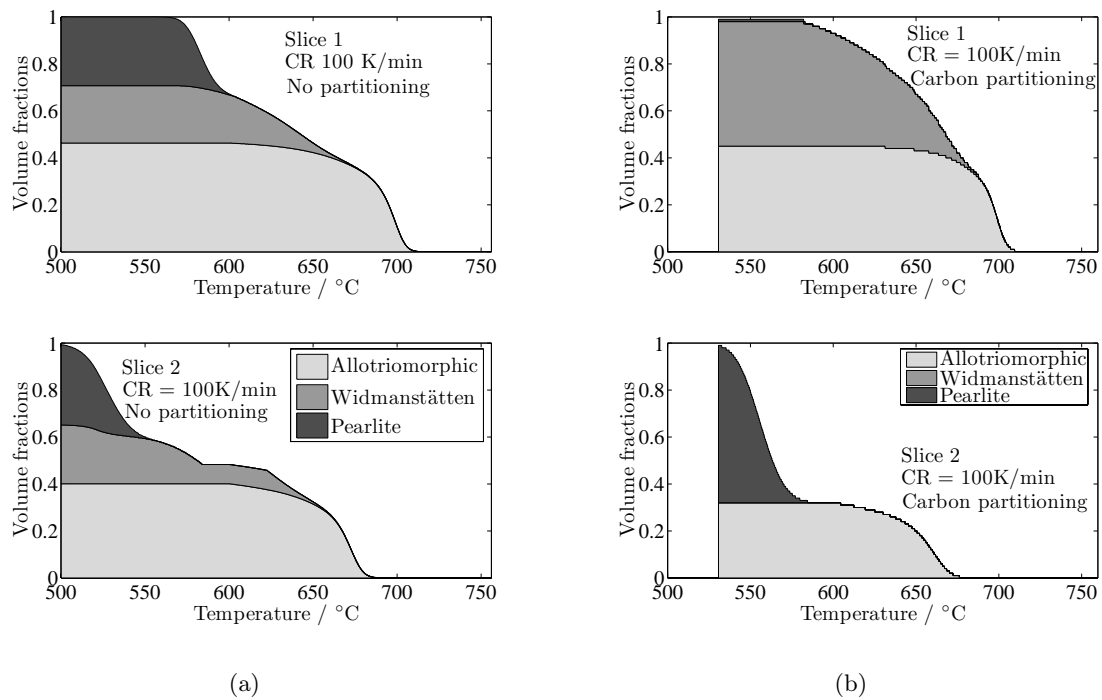


Figure 3.1.: Accumulated volume fractions of all phases versus temperature for calculations using the “standard” set of input parameters and a cooling rate of  $100 \text{ K min}^{-1}$ . (a) for a calculation without carbon partitioning, i.e. for independent slices and (b) for a calculation with carbon partitioning, i.e. for interacting slices.

Figure 3.2(a) to (d) show similar results as figure 3.1(b). In slice 1 (low manganese concentration), allotriomorphic ferrite is formed and, with increasing cooling rate, also Widmanstätten ferrite. Slice 2 consists of allotriomorphic ferrite and pearlite. An unexpected result is the occurrence of pearlite in slice 1 for a cooling rate of  $12.5 \text{ K min}^{-1}$ . This is a reproducible effect that does not depend on the length of the lime step. But as the total volume fraction is only 4% (as opposed to 1% in other calculations) and as slower and faster cooling rates do not show pearlite in slice 2, this was treated as an outlier. For a cooling rate of  $200 \text{ K min}^{-1}$  (figure 3.3(b)), phase transformations were not complete at  $500^\circ\text{C}$ , which indicates that the resulting microstructure is partly martensitic. At  $800 \text{ K min}^{-1}$ , slice 1 was not fully transformed at  $500^\circ\text{C}$  as well. No pearlite was formed at all. The volume fraction of each phase that is formed can be seen in figure 3.4. With increasing cooling rate, less allotriomorphic ferrite is formed in both slices, but the other two phases show a more complicated behaviour. For Widmanstätten ferrite in slice 1 and pearlite in slice 2, the phase fraction increases with the cooling rate, but then drops above  $100 \text{ K min}^{-1}$  and  $200 \text{ K min}^{-1}$ , respectively. This drop happens at the same cooling rate for which transformation is not complete for the first time. It can therefore be concluded that the model predicts an increasing fraction of pearlite and Widmanstätten ferrite with increasing cooling rate, but that growth of these two phases is prevented by the termination of the phase transformation when the temperature falls below  $500^\circ\text{C}$ . The fractions of Widmanstätten ferrite in slice 2 and of pearlite in slice 1 are very low throughout the cooling rate range.

There is an increasing amount of pearlite in slice 2 with increasing cooling rate while the total amount of ferrite stays at nearly 100%. This indicates that banding becomes more pronounced with increasing cooling rate. When transformation is shifted to low temperatures, pearlite formation is suppressed and a ferritic/martensitic microstructure results. This is also true when the program is allowed to continue under  $500^\circ\text{C}$ . In figure 3.1(c), the results for such calculations are presented. At  $200 \text{ K min}^{-1}$  the transformation still reaches 100%, but for cooling rates that are higher, no pearlite forms and the microstructure is predicted to be partly martensitic. So the program shows the expected elimination of banding at high cooling rates if or if not the transformation is terminated at  $500^\circ\text{C}$ . The critical cooling rate at which banding is suppressed, however, does depend on whether the program is artificially terminated at  $500^\circ\text{C}$  and also on the subroutine PEARL which is potentially unreliable at low temperatures and high manganese contents. It would be interesting to repeat these calculations with a model that takes carbon diffusion at finite diffusivity into account. This should have a considerable influence on the critical cooling rate, too.

The continuous cooling diagrams of figure 3.5 summarise these results. They show typical curves with start temperatures for all phases decreasing with increasing cooling rate. Transformation in slice 2 generally takes place at slightly lower temperatures than slice 1 and is finished at lower temperatures, too. Widmanstätten ferrite forms in slice 1 at higher temperatures and in larger amounts than in slice 2. Pearlite formation, on the other hand, starts only directly before the phase transformation is completed in slice 1. In both slices, pearlite formation is completely suppressed at cooling rates higher than  $200 \text{ K min}^{-1}$ . To see full C-curves in this diagram, it would have been necessary to conduct calculations at higher cooling rates and with a model that can reliably describe transformation at temperatures below  $500^\circ\text{C}$ .

In figure 3.6, the estimated ferrite grain size is drawn as a function of the cooling rate. It is generally larger for slice 2 than for slice 1. While it almost stays constant with increasing cooling rate in slice 1, it drops sharply from over  $90 \mu\text{m}$  at  $1 \text{ K min}^{-1}$  to about  $10 \mu\text{m}$  at  $50 \text{ K min}^{-1}$  in slice 2. This is expected, because a higher cooling rate leaves the existing nuclei less time to grow into untransformed regions before new nuclei are formed. Thus, more nuclei are “successful” and

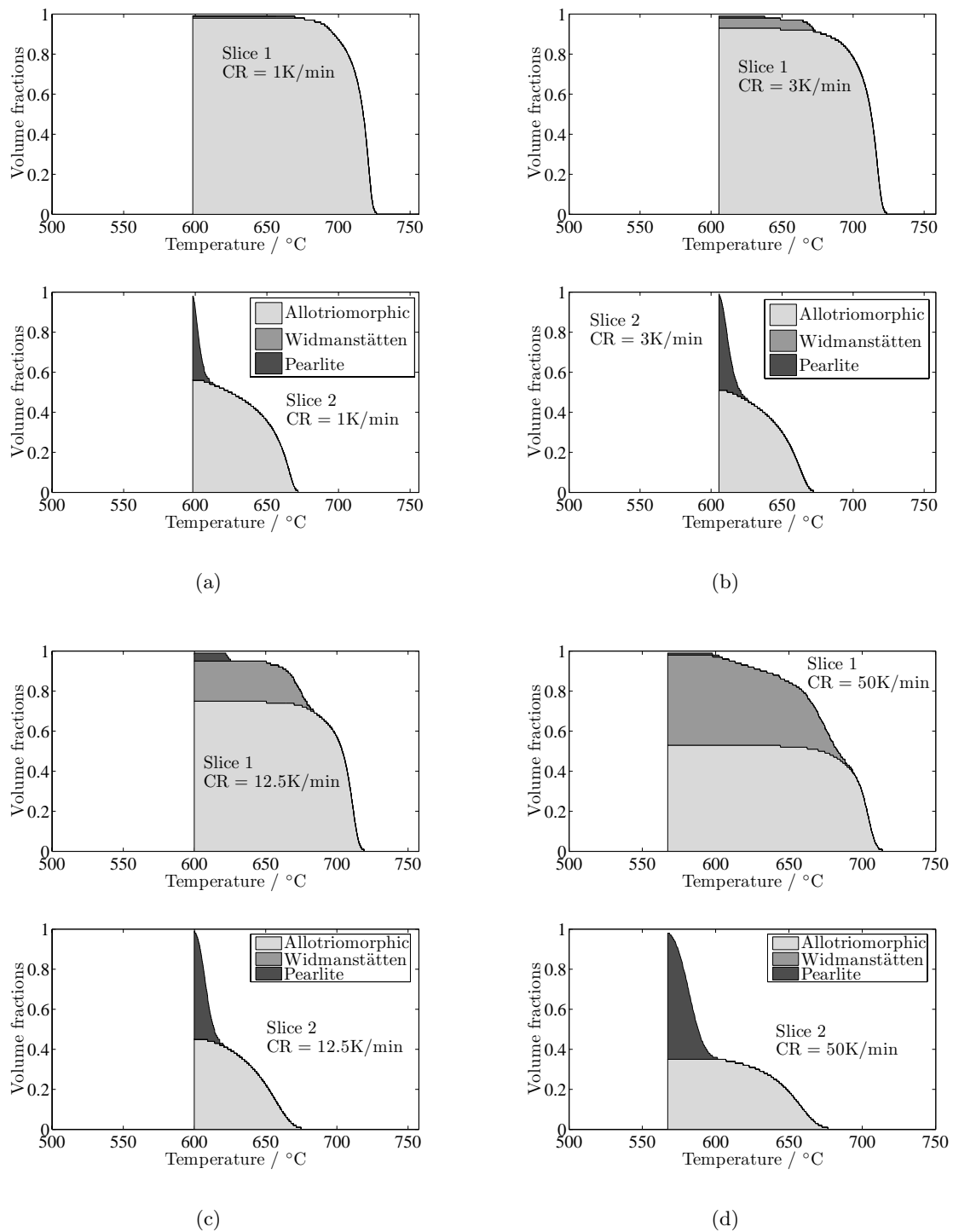


Figure 3.2.: Accumulated volume fractions of all phases as a function of temperature for both slices and various cooling rates between 1 and 50 K min<sup>-1</sup>.

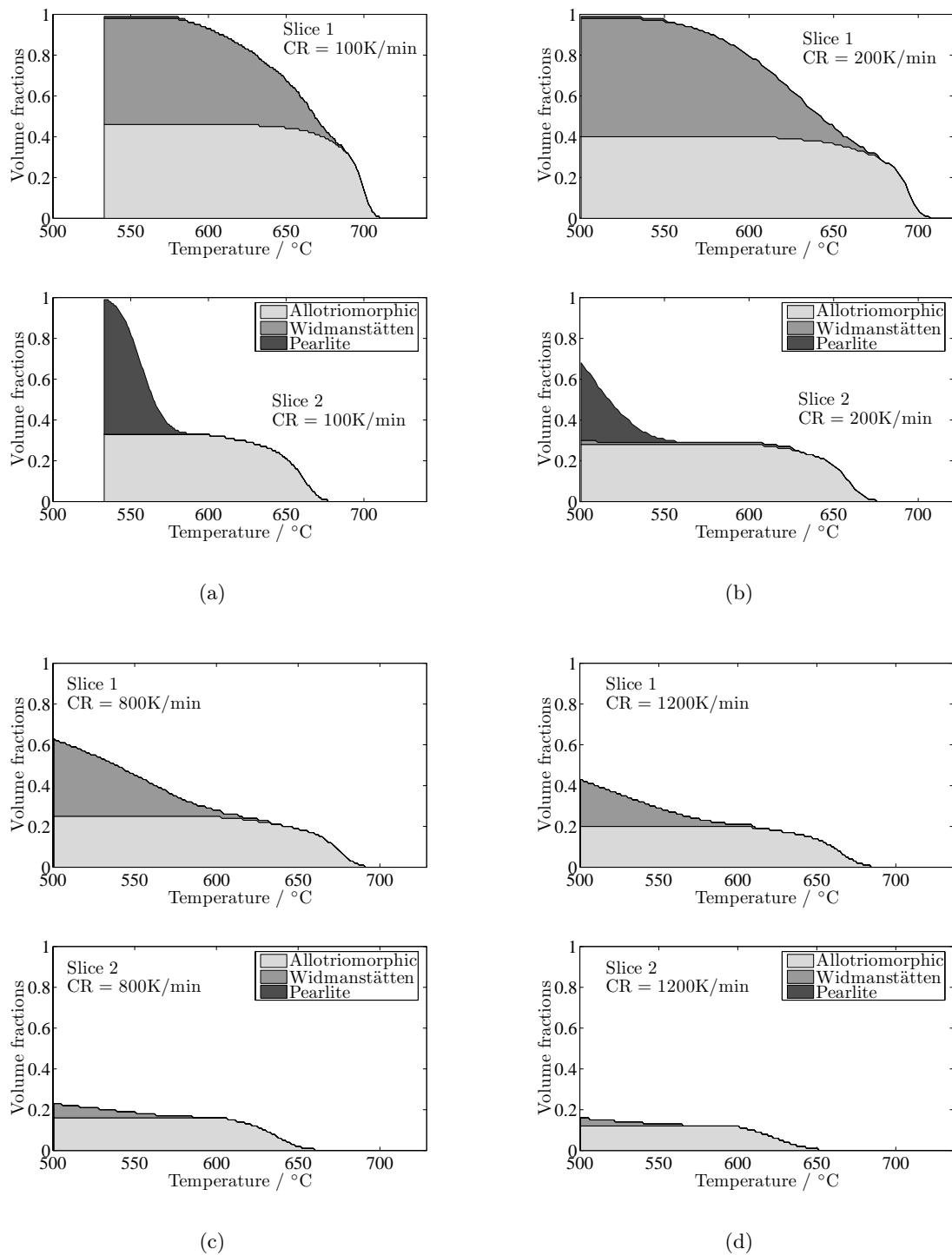


Figure 3.3.: Accumulated volume fractions of all phases as a function of temperature for both slices and various cooling rates between 100 and 1200 K min<sup>-1</sup>.

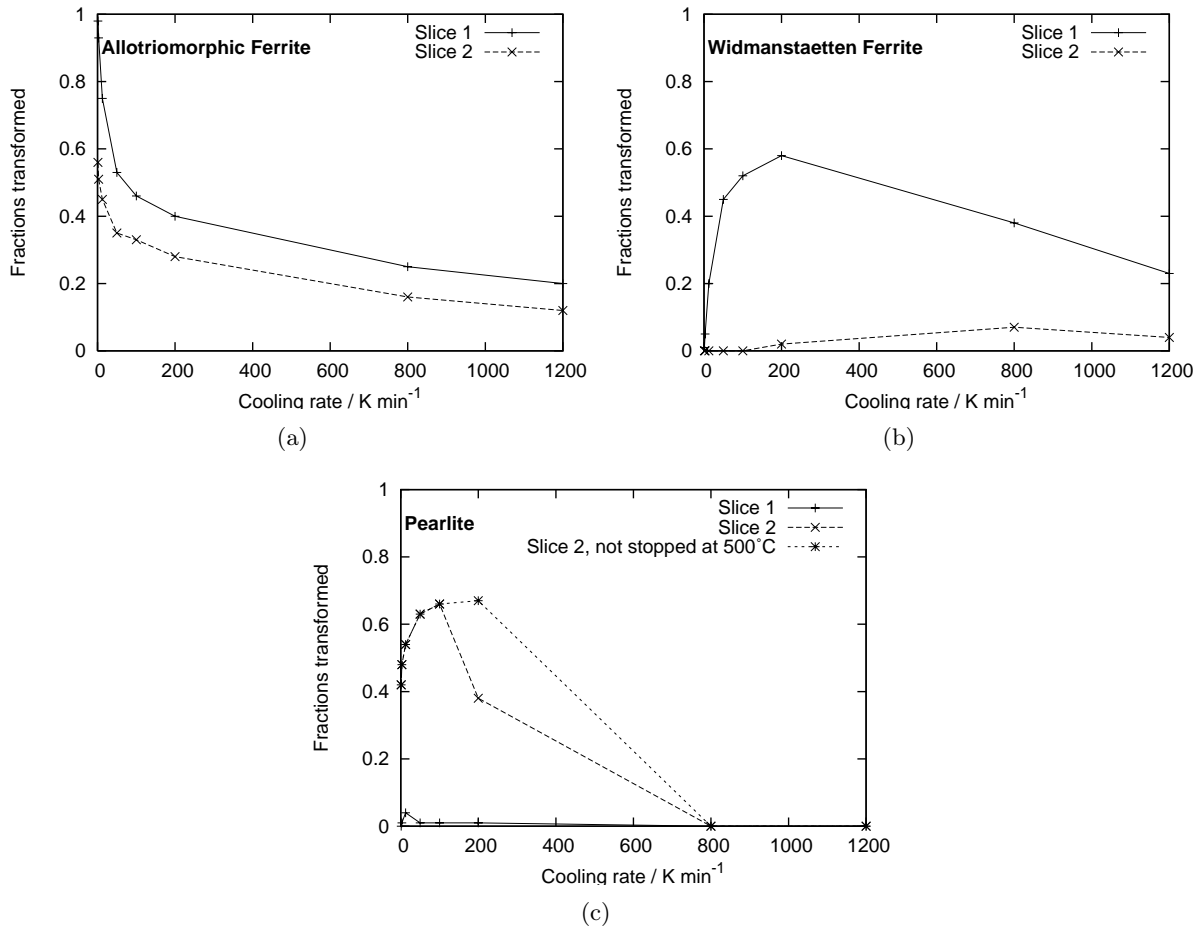


Figure 3.4.: Final volume fractions as a function of cooling rate for both slices and all phases. In (c), the volume fraction of pearlite that results when the calculation is not stopped at 500°C is shown additionally.

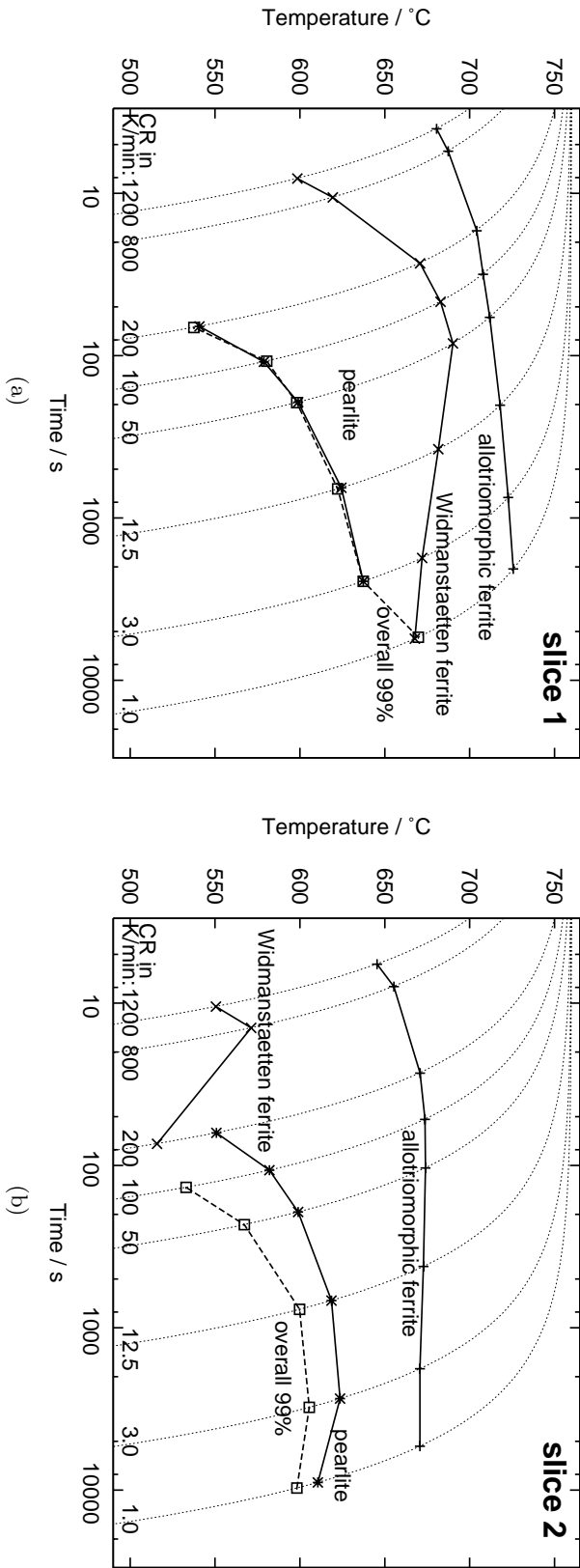


Figure 3.5.: Continuous cooling diagrams of calculations using the “standard” set of input parameters and different cooling rates (CR). Shown are the times and temperatures at which 1% of the total volume was transformed into the various phases in slice 1 (a) and slice 2 (b). Also shown is the point at which transformation was finished, indicated by an overall transformed fraction of 99% in the respective slice.

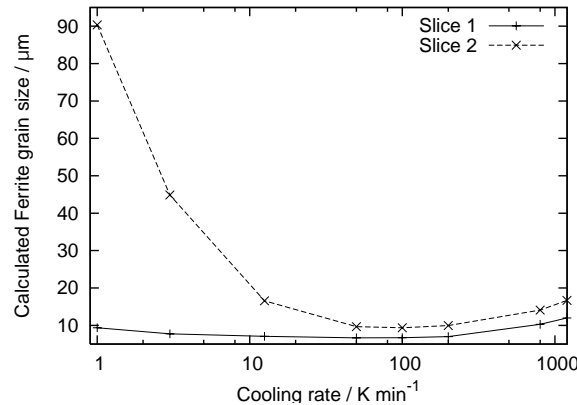


Figure 3.6.: Calculated ferrite grain size versus cooling rate for both slices. Note the logarithmic scale.

the average grain size decreases. The fact that the grain size starts to increase again for cooling rates of  $200 \text{ K min}^{-1}$  and higher is probably not a physical effect, but rather a result of the way in which the grain sizes were calculated: The number of “successful” nuclei determines the ferrite grain size. At high cooling rates, the transformation does not proceed to 100% and therefore the number of nuclei is lower than for complete transformation, leading to an apparently larger grain size.

### 3.1.3. Austenite Grain size

In the absence of a length scale in the current model, the only influence that changing the average austenite grain size has is on the grain boundary area per unit volume and thus on nucleation. The austenite grain size was varied between 1 and  $200 \mu\text{m}$ . The results of the calculations are displayed in figure 3.7. It can be seen that the volume fraction of allotriomorphic ferrite decreases with increasing austenite grain size. As allotriomorphic ferrite nucleates on grain boundaries and an increasing austenite grain size means a decreasing grain boundary area, this behaviour is expected. The volume fraction of Widmanstätten ferrite, on the other hand, increases with increasing austenite grain size. When less allotriomorphic ferrite is formed, there is less carbon enrichment in the untransformed austenite. This in turn favours the formation of Widmanstätten ferrite and explains the observed increase with austenite grain size. The volume fraction of pearlite in slice 1 is very low for all grain sizes (with the exception of  $10 \mu\text{m}$ ), but for slice 2 it increases with austenite grain size at first, reaches a maximum at  $50 \mu\text{m}$  and falls slightly for grain sizes larger than this. This behaviour is exactly the opposite of the total amount of ferrite formed. The less ferrite is formed in one slice, the more austenite transforms into pearlite and vice versa.

Figure 3.8 shows the estimated average ferrite grain size as a function of the input average austenite grain size. If the first datum is ignored, the ferrite grain size rises steadily with increasing austenite grain size, but is always clearly smaller than it. Ferrite grains in slice 2 are slightly larger than in slice 1, probably because transformation to ferrite takes place at lower temperatures where the nucleation rate is lower. The increase of ferrite grain size with austenite grain size is expected because an increase in austenite grain size decreases the grain boundary area per volume available for nucleation and hence the total number of nuclei, leading to larger grains. The first

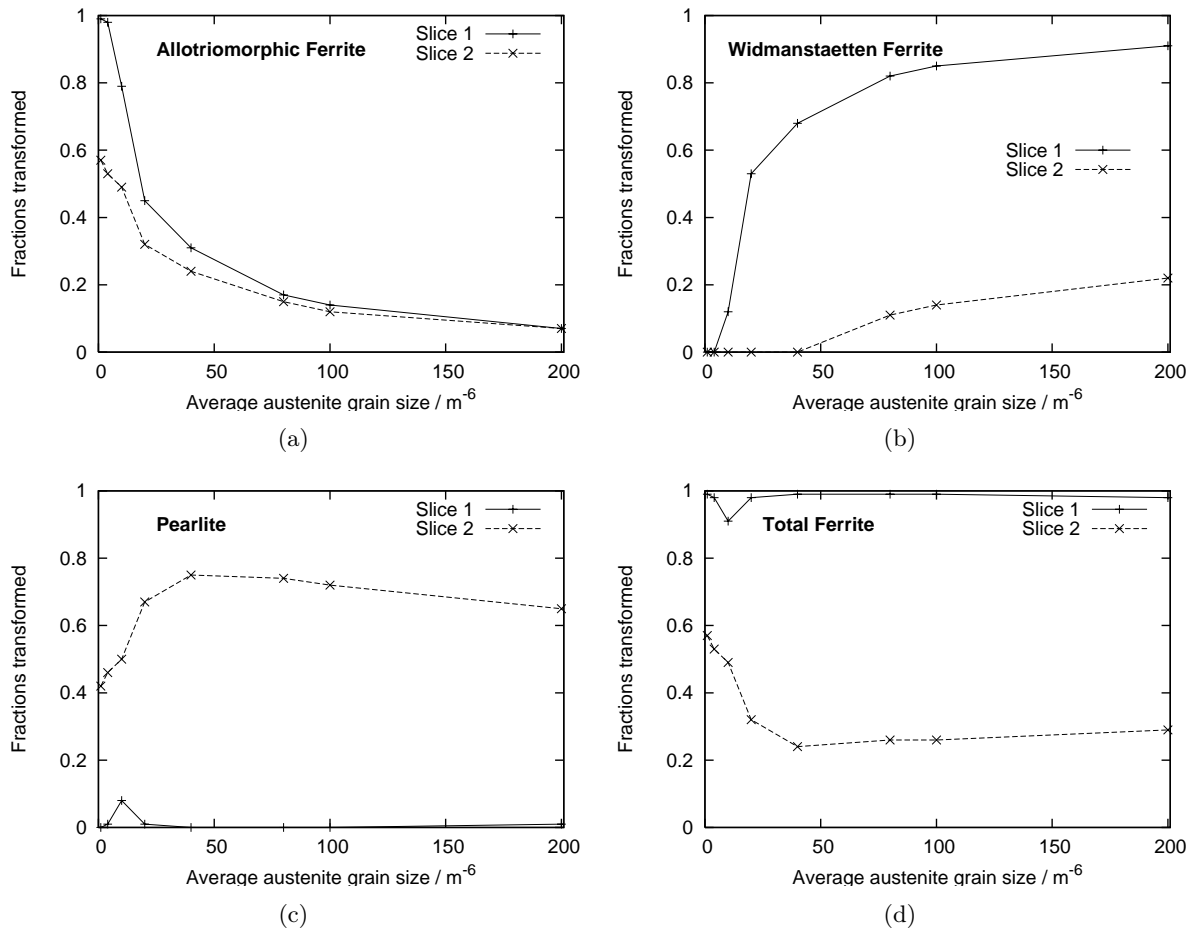


Figure 3.7.: Final volume fractions as a function of austenite grain size for both slices and all phases as well as (d) the sum of allotriomorphic and Widmanstätten ferrite.

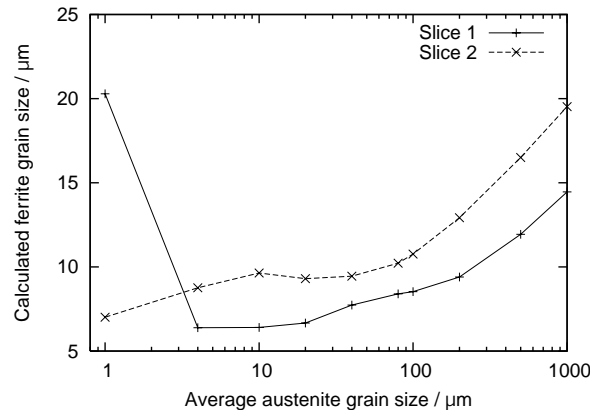


Figure 3.8.: Calculated ferrite grain size versus original austenite grain size for both slices

data point, however, that shows a dramatically larger ferrite grain size than all other points, cannot be explained with this reasoning. It is treated as an outlier.

### 3.1.4. Concentration Fluctuation Amplitude

The concentration fluctuation amplitude  $\Delta C_{\text{Mn}}$  was varied from 0.01 wt.-% to 1.49 wt.-%. This means that the manganese concentration ranged from 1.49 to 1.51 wt.-% in the case of the smallest fluctuation and from 0.01 to 2.99 wt.-% in the case of the largest fluctuation. As in the sections before, the final transformed fractions are plotted versus the concentration amplitude for both slices and all three phases. Figure 3.9(a) shows that the difference between the fractions of allotriomorphic ferrite in the two slices increases with increasing concentration fluctuation amplitude. The same holds for pearlite (figure 3.9(c)) until a fluctuation amplitude of 0.9 wt.-%, which indicates that there is more banding the higher  $\Delta C_{\text{Mn}}$  is. Above an amplitude of 0.3 wt.-%, there is no pearlite at all in slice 1 after finished transformation. This means that above this value, all carbon precipitation must take place in slice 2. At the same concentration fluctuation amplitude, the fraction of Widmanstätten ferrite content in slice 1 reaches reaches a maximum. It had risen from 20% to above 40%, but levels off and even drops slightly at values above 0.3 wt.-%. This curve can be understood by considering the fraction of allotriomorphic ferrite in slice 1: it remains almost constant. The fewer pearlite is formed in slice 1, the more Widmanstätten ferrite can replace it. At high concentration fluctuation amplitudes, where no pearlite at all is present in slice 1, Widmanstätten can only form in the untransformed fraction that is not already occupied by allotriomorphic ferrite. For concentration fluctuations amplitudes above 0.9 wt.-%, the fraction of pearlite falls sharply. A higher amplitude means that more pearlite can be formed in slice 2, but also that the transformation is shifted to lower temperatures. Above this value, pearlite formation is shifted to temperatures below 500°C, which means that it cannot take place any more. Therefore, the fraction of pearlite drops rapidly and martensite is formed instead. These graphs show how ferrite/pearlite banding develops with increasing concentration fluctuation amplitude, becomes more pronounced and is finally replaced by ferrite/martensite banding.

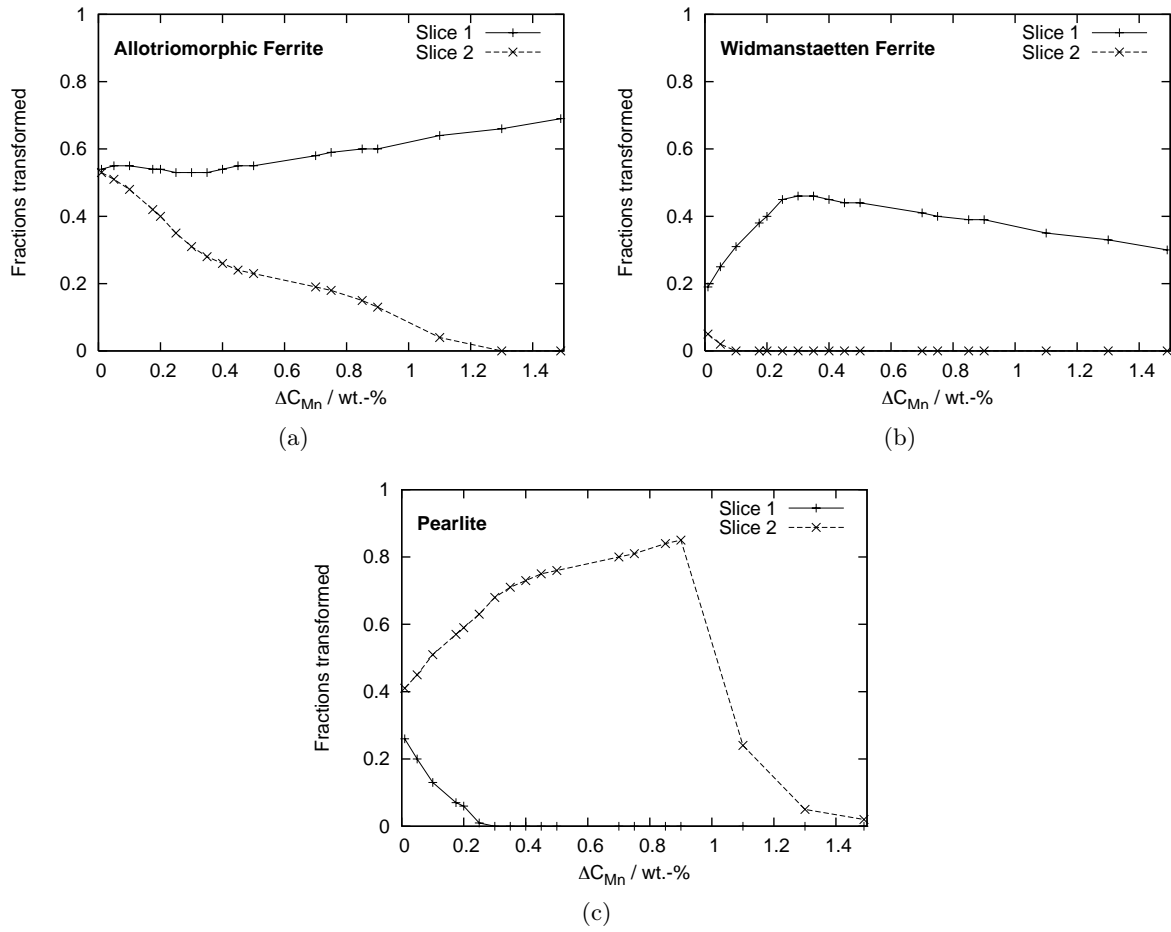


Figure 3.9.: Final volume fractions as a function of the manganese fluctuation amplitude for both slices and all phases

## 3.2. Comparison with Results from the Literature

After testing the general behaviour of the program, it was attempted to reproduce experimental data. Two test cases were selected. The first was taken from Kirkaldy et al. [1], the second from Caballero et al. [2]. Both papers study the occurrence of banding as a function of cooling rate under isochronal conditions (constant cooling rate). While Kirkaldy et al. studied an “artificially banded” material, Caballero et al. used a dual phase steel.

### 3.2.1. Test Case “A”: Kirkaldy et al. [1]

The article [1] was an important contribution to the understanding of the banding phenomenon. As described in section 1.1.1, Kirkaldy et al. used three discs of different manganese concentration welded together to simulate banding. The middle disc had a Mn-Concentration of 3.3 wt.-% while the two discs on each side were manganese-free. A calculation with two slices has exactly the same setup as the experiment (if mirror symmetry is taken into account). All used input parameters for the calculations are listed in table 2.3 under input set “A”. Unfortunately, Kirkaldy et al. [1] do not state the austenite grain size before transformation, so a standard value of  $20\ \mu\text{m}$  was used. The cooling rates reported in the paper are 1.2, 4.0, 7.5 and  $50.0\ \text{K min}^{-1}$ . Additionally, calculations with a cooling rate of 15, 20, 30 40 and  $75\ \text{K min}^{-1}$  were conducted.

The original micrographs from [1] are shown in figure 3.10. It can be seen that banding occurs for cooling rates up to  $7.5\ \text{K min}^{-1}$ . For a cooling rate of  $50\ \text{K min}^{-1}$ , the microstructure of the high-manganese part of the sample (the middle part) seems to be fully martensitic and banding is suppressed. The results of the calculations are presented in figures 3.11 and 3.12. Due to the very high concentration fluctuation amplitude, the results are quite extreme: For low cooling rates, slice 1 consists entirely of allotriomorphic ferrite while slice 2 contains only pearlite. When the cooling rate is increased, a part of the allotriomorphic ferrite in slice 1 is replaced by Widmanstätten ferrite, but there is still no pearlite at all in this slice. In slice 2, on the other hand, the volume fraction of pearlite falls rapidly for cooling rates higher than  $7.5\ \text{K min}^{-1}$ . until it reaches reaches zero at  $50\ \text{K min}^{-1}$ . The reason for this behaviour can be seen in figure 3.11. For high cooling rates, pearlite formation is shifted to lower temperatures and eventually would have to take place below  $500^\circ\text{C}$ . Pearlite cannot form at these low temperatures and slice 2 instead consists of martensite. This is exactly what Kirkaldy et al. describe in their paper. In these calculations, the critical cooling rate for which pearlite formation was suppressed could be reproduced correctly.

It must be noted that these calculations were done using a very high manganese concentration in one slice (3.3 wt.-%) and no manganese at all in the other slice. As mentioned in section 2.3.3, some empirical equations used by subroutine PEARL are only valid for manganese concentrations up to 1.8 wt.-%, possibly leading to inaccurate results for Mn-concentrations above this level.

### 3.2.2. Test Case “B”: Caballero et al. [2]

The second test case was taken from a paper by Caballero et al. [2]. They annealed a dual phase steel at  $1200^\circ\text{C}$  before hot rolling it. Beginning at  $900^\circ\text{C}$ , it was cooled down with constant cooling rates of  $420\ \text{K min}^{-1}$  and  $3600\ \text{K min}^{-1}$  to  $500^\circ\text{C}$  and subsequently coiled at this temperature. Micrographs taken after cooling to room temperature of samples treated with the two different cooling rates are shown in figure 3.13. They show that “samples cooled at  $420\ \text{K min}^{-1}$  [...] exhibit a ferrite and pearlite microstructure” while “samples more rapidly cooled [...] consist

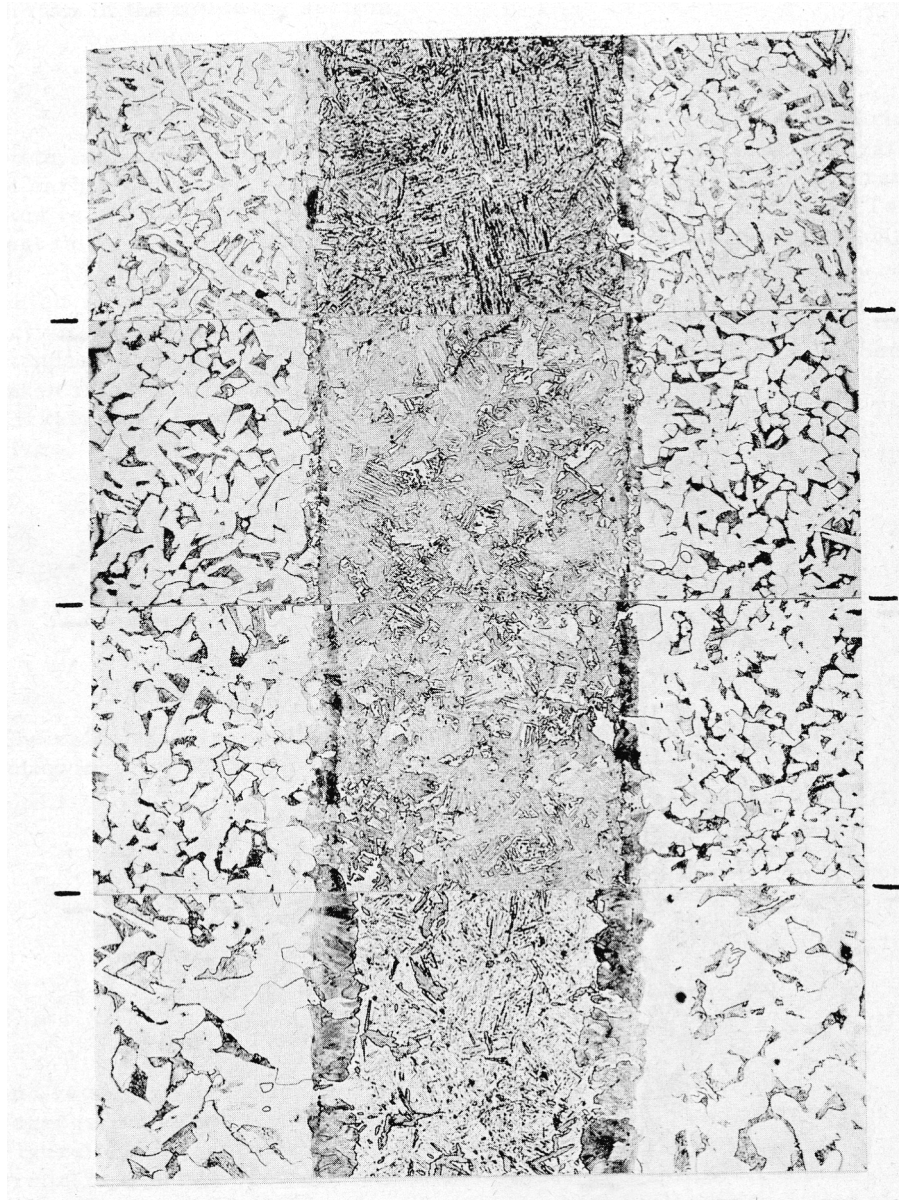


Figure 3.10.: Light optical micrographs from [1] showing the microstructure of diffusion couples. From top to bottom cooling rate  $50 \text{ K min}^{-1}$ ,  $7.5 \text{ K min}^{-1}$ ,  $4.0 \text{ K min}^{-1}$  and  $1.2 \text{ K min}^{-1}$ . Magnification  $\times 53.5$ .

### 3.2. Comparison with Results from the Literature

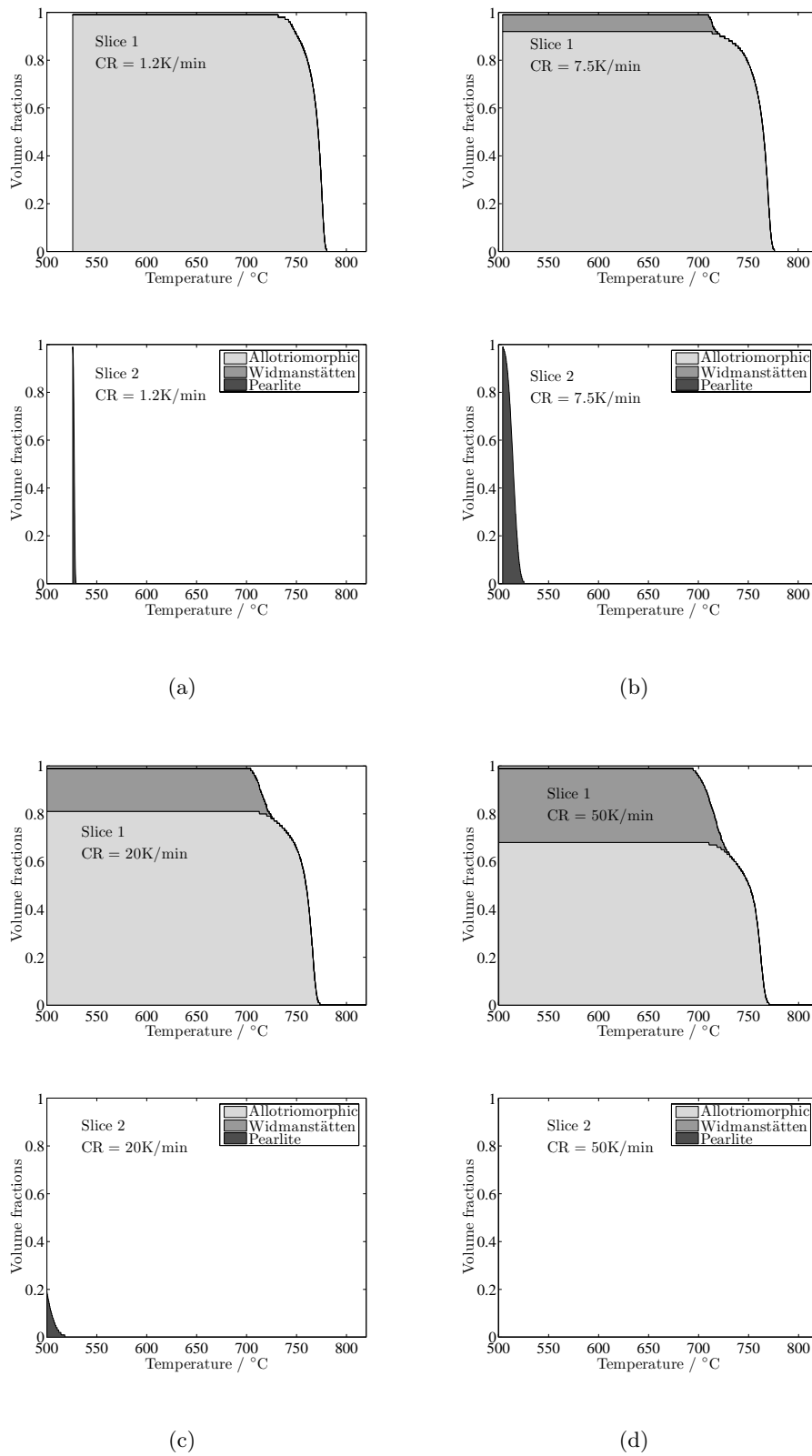


Figure 3.11.: Accumulated volume fractions of all phases as a function of temperature for both slices and various cooling rates for set “A” of input parameter.

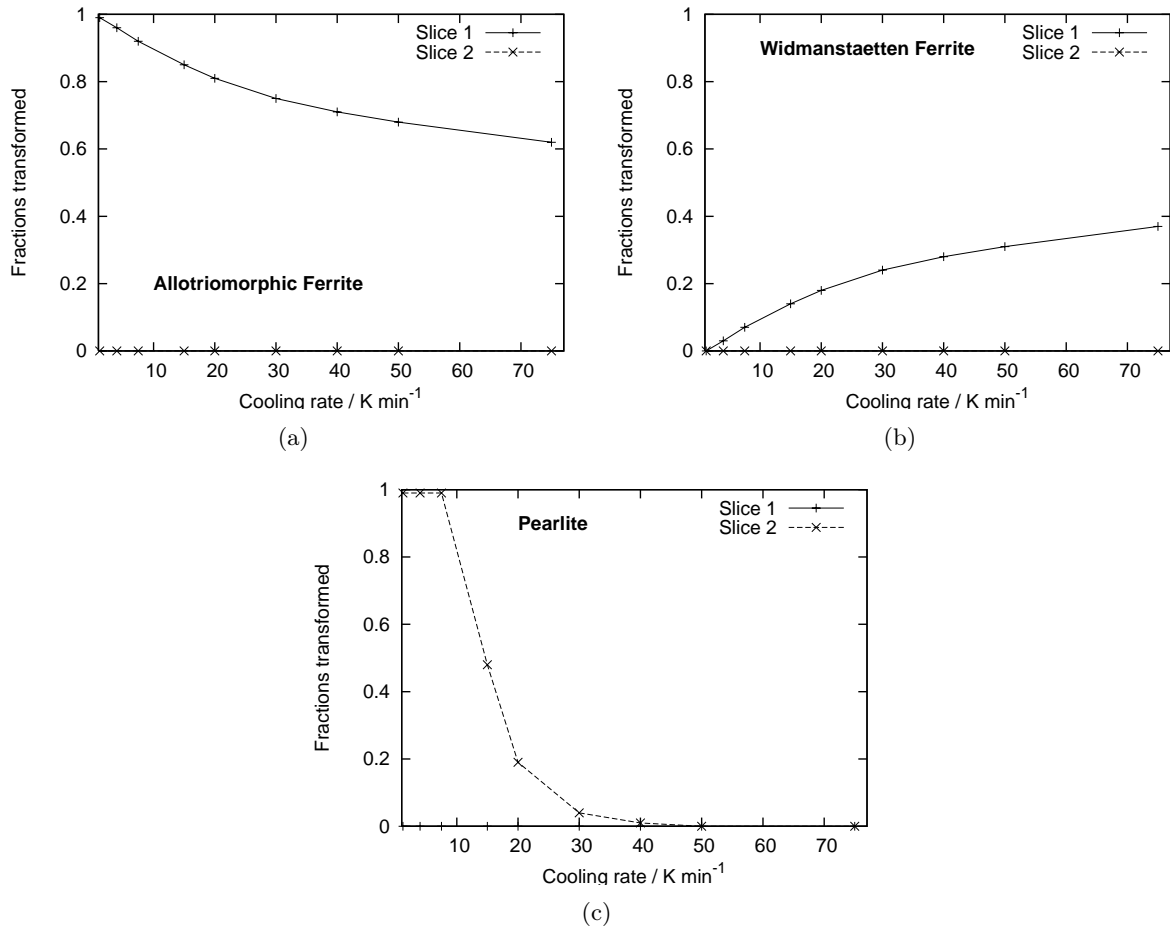


Figure 3.12.: Final volume fractions as a function of cooling rate for both slices and all phases for set “A” of input parameter.

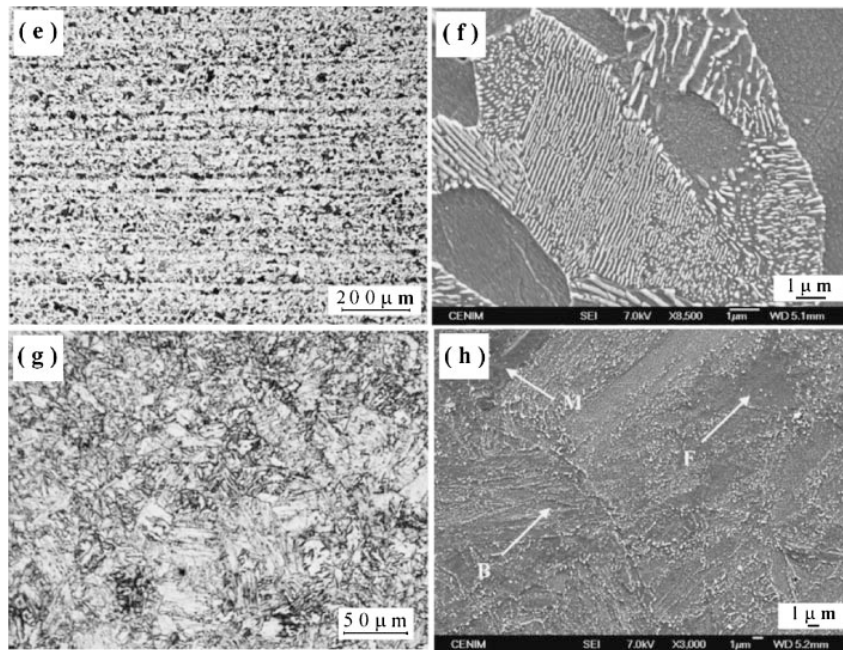


Figure 3.13.: Micrographs taken from [2] showing the microstructure of hot rolled specimens. (e) and (f) show specimens cooled with a cooling rate of  $420 \text{ K min}^{-1}$ , (g) and (h) show specimens cooled with a cooling rate of  $3600 \text{ K min}^{-1}$ . Light optical micrographs (e) and (g), electron micrographs (f) and (h). B means bainite, M is martensite, F is ferrite and P is pearlite.

of mainly bainite and martensite” [2, p. 2270]. The authors conclude from these results that banding can be suppressed by increasing the cooling rate.

Calculations were carried out using set “B” of input parameters. The original austenite grain size and the present concentration fluctuation amplitude could not be taken from the literature, so standard values of  $20 \mu\text{m}$  and  $\pm 0.25 \text{ wt.-%}$  were assumed. Calculations with different austenite grain sizes and fluctuation amplitudes were performed as well, but did not lead to significantly different findings. Additional to the two cooling rates used in the experiments, lower values were used as well. Results of the simulations are displayed in figures 3.15 and 3.14. Both figures show expected results. At low cooling rates, pearlite and allotriomorphic ferrite dominate in slice 2 while slice 1 mainly consists of allotriomorphic and Widmanstätten ferrite. At cooling rates higher than  $60 \text{ K min}^{-1}$ , pearlite cannot form any more because transformation would take place below  $500^\circ\text{C}$ . The microstructure in both slices consists of ferrite and martensite, although the fraction of ferrite is much higher in slice 1 than in slice 2. At a cooling rate of  $3600 \text{ K min}^{-1}$ , almost the entire microstructure consists of martensite, i.e almost no transformation took place until  $500^\circ\text{C}$ .

The findings qualitatively agree with experimental results, although the model cannot deal with the formation of bainite. However, the simulations predict that almost the entire microstructure of a specimen cooled at  $3600 \text{ K min}^{-1}$  should consist of martensite, while experiments show that at this cooling rate, only a small part of the microstructure is martensitic. It can therefore be concluded that the model can qualitatively predict experimental behaviour, but to achieve

quantitative agreement, further detail would have to be included into the program and possibly input parameters would have to be adjusted.

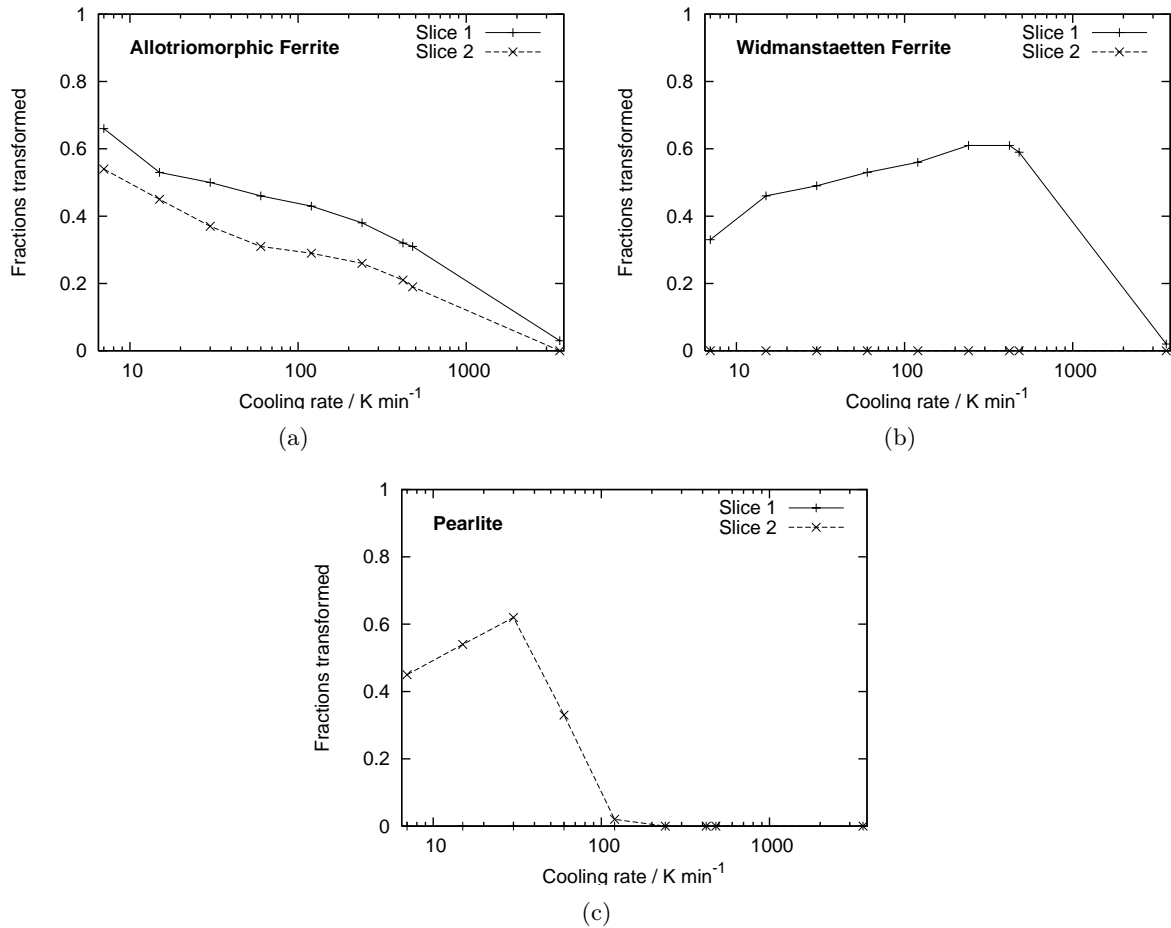


Figure 3.14.: Final volume fractions as a function of cooling rate for both slices and all phases for set “B” of input parameter. Note the logarithmic scale.

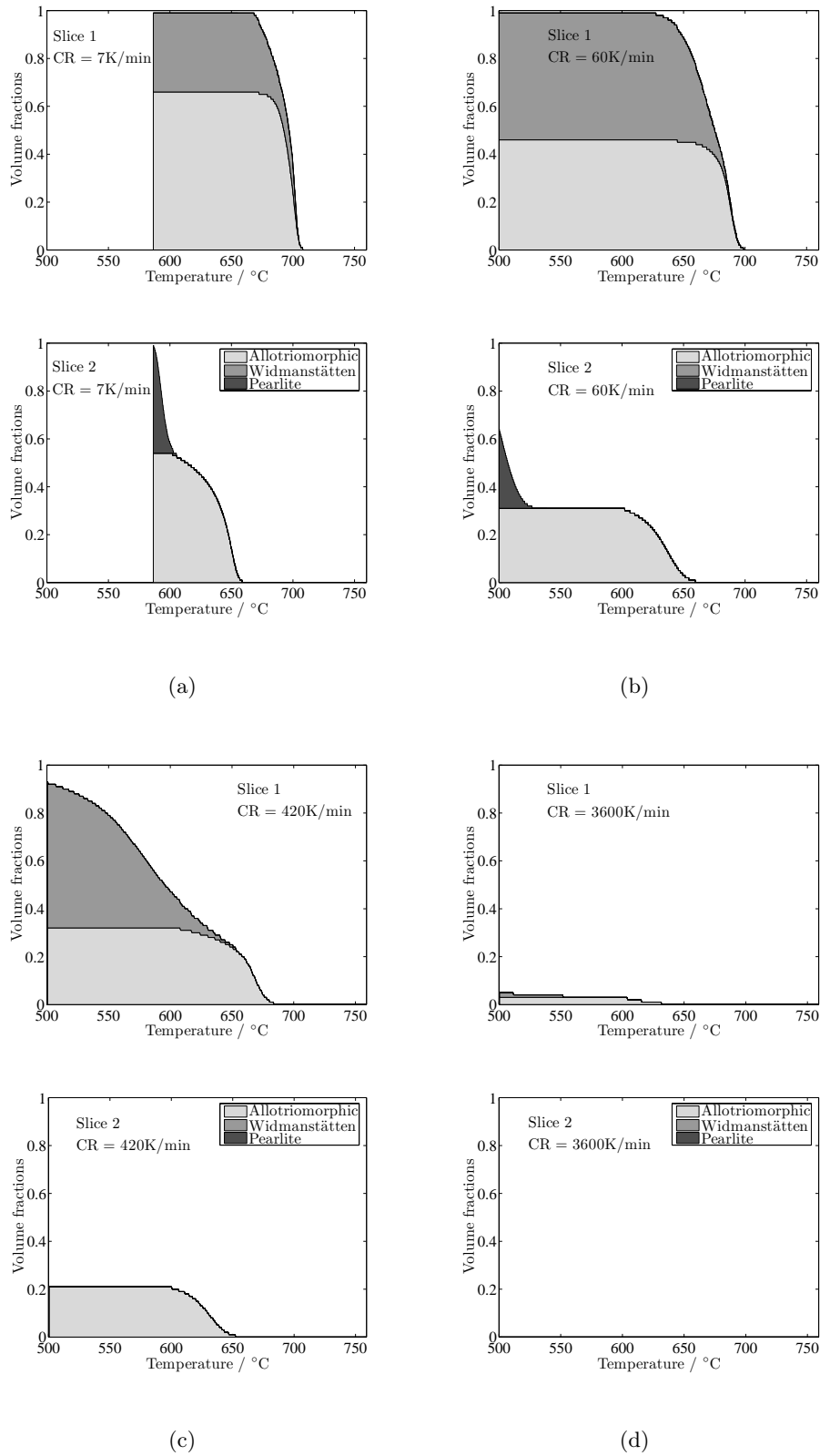


Figure 3.15.: Accumulated volume fractions of all phases as a function of temperature for both slices and various cooling rates for set “B” of input parameter.

## Chapter 4.

# Conclusions and Further Work

The model created is generally able to describe the behaviour of steels exhibiting banding, although it uses a number of quite simple approximations. One of the main limitations of the current model is that even though concentration slices have been introduced, it is still a continuum calculation. To capture effects generated by the segregation profile width (the concentration fluctuation wavelength) or the ratio of the austenite grain size to the fluctuation wavelength as explained in section 1.1.2, a length scale needs to be introduced, making the continuum model one dimensional. In most calculations, the microsegregation profile was approximated by two concentration slices. Although this is enough to predict banding, it may be too crude a model to accurately describe reality. A larger slice number needs to be employed with more sophisticated concentration profile shapes as discussed in section 2.3.2. The choice of the right function describing the segregation profile can have a considerable influence on the simulation results, especially if it would be attempted to predict the band width. A key limitation of the model is the assumption of infinitely fast carbon partitioning between the slices. This problem will be discussed further below.

The results of calculations in which input parameters were varied systematically can be summarised as follows: Banding becomes more pronounced with increasing cooling rate, but above a certain critical cooling rate, pearlite is replaced by martensite in the high-manganese slice, and at even higher cooling rates, the whole microstructure consists of martensite and banding is hence suppressed. The same trend holds for increasing concentration fluctuation amplitude. At a low amplitude, banding is not clearly visible but it becomes more and more marked until, above a critical amplitude, pearlite formation is suppressed and a ferrite/martensite microstructure results. When the input average austenite grain size is increased, banding is not eliminated. Allotriomorphic ferrite is replaced with Widmanstätten ferrite with increasing austenite grain size, but the ferrite/pearlite microstructure persists. The average ferrite grain size after transformation increases with increasing austenite grain size because larger austenite grains lead to less ferrite nucleation. The austenite grain size has no other effect in the current model.

It was attempted to reproduce experimental results taken from the literature. In one case (section 3.2.1), the critical cooling rate for the suppression of banding could be reproduced quantitatively, while in the second case (section 3.2.2), it was only possible to reproduce the trend qualitatively. The cooling rates involved in the second case were much higher than in the first case, which is probably the reason why the results weren't as precise. At high cooling rates, the assumption of infinitely fast carbon partitioning is unrealistic. The model needs to be improved in this respect. It would also be interesting to eventually include bainite formation into the program although this is of minor consequence to the vast majority of banded steels.

---

The simplest way to include a realistic carbon partitioning velocity into the model is to use Fick's first law (in one dimension):

$$J = -D_S \frac{\Delta C}{\Delta x} \quad (4.1)$$

Here,  $J$  denotes the carbon flux,  $D_S$  the carbon diffusion coefficient in austenite and  $\frac{\Delta C}{\Delta x}$  the carbon concentration gradient. When two manganese concentration slices are used, the calculation is straightforward. The carbon enrichment in each slice can be calculated independently at each time step after transformation and the carbon concentration gradient is simply given by the difference of these concentrations divided by the slice width (the concentration fluctuation wavelength). When the carbon flux is known, the amount of carbon that partitions is calculated by multiplying the flux with the time step  $\Delta t$ . The new carbon concentration in each slice equals the old one plus the amount of carbon diffused. However, it must be checked first if the amount of diffusing carbon is larger than that necessary to reach an equal carbon concentration in both slices. If it is, the carbon concentration in all slices can be calculated using the assumption of infinitely fast partitioning. If more than two slices are used, the flux in each slice must be calculated and the amount of carbon diffusing is the sum of the amount of carbon diffusing out of this slice and the amount of carbon diffusing into the slice from adjacent ones.

When the above modification to the program is made, the concentration fluctuation wavelength is needed as an input. Thus, a length scale is introduced in the program and it becomes possible to study the influence of the segregation profile width as mentioned above. Also, a band width can be defined by considering the amount of pearlite in each slice as a function of slice number. This banding wavelength can then be used as additional output and can be compared with literature data.

Even without the proposed modifications, the model presented in this thesis has proven to be a useful tool for studying microstructural banding in steel.

# Appendix A.

## FORTRAN-Program

This appendix contains the description of the program that is given on the Materials Algorithm Project website at <http://www.msm.cam.ac.uk/map/mapmain.html>. The source code of the program as well as example input and output files can be downloaded there.

### **Materials Algorithms Project**

#### **Program Library**

Program MAP\_STEEL\_BANDING

#### **Provenance of Source Code**

E. A. Jäggle and H.K.D.H. Bhadeshia,  
Phase Transformations Group,  
Department of Materials Science and Metallurgy,  
University of Cambridge,  
Cambridge, U.K.

#### **Purpose**

To calculate the microstructure (ferrite, Widmanstatten ferrite and pearlite) of steel as a function of the chemical composition, cooling rate and austenite grain size for a sample with inhomogeneous manganese concentration leading to microstructural banding.

#### **Specification**

The program is self-contained.

Language: FORTRAN

Product form: Source code

#### **Description**

This program is a derivative of the program MAP\_STEEL\_STRUCTURE by Jones and Bhadeshia. The microstructure is calculated as described in detail in the references below.

#### **References**

This thesis and [53, 55, 66].

#### **Input parameters**

These are all listed in the input file TESTINPUTDATA, contained in the bundle that can be downloaded from the MAP website and in section 2.3 of this thesis.

#### **Output parameters**

The temperature, time, carbon concentration of the residual austenite and volume fractions of allotriomorphic ferrite, Widmanstatten ferrite, pearlite at all concentration steps and time steps as described in section 2.4 of this thesis.

#### **Download**

of the bundle under <http://www.msm.cam.ac.uk/map/steel/tar/banding.tar>

## Appendix B.

### Example Input File

A typical input file, in this case for a calculation with “standard” composition. All parameters are explained in section 2.3.

```
0.2 CARBON
0.2 SILICON
1.5 MANGANESE
0.0 NICKEL
0.0 MOLYBDENUM
0.0 CHROMIUM
0.0 VANADIUM
20.0d-6 EQUIAXED AUSTENITE GRAIN SIZE
2 HEAT TREATMENT USED (2: CONTINUOUS COOLING RATE)
12.5 LINEAR COOLING RATE IN K min-1
0.5 TIME STEP
50000 MAXIMUM NUMBER OF ITERATIONS
0.25 MANGANESE FLUCTUATION AMPLITUDE
2 NUMBER OF SLICES
0.022D0 AUSTENITE FERRITE INTERFACIAL ENERGY
200.0 ACTIVATION ENERGY FOR ATOMIC TRANSFER
0.333 SHAPE FACTOR FOR BOUNDARY NUCLEATION
1.0d-8 FRACTION OF EFFECTIVE BOUNDARY SITES
0.45 SHAPE FACTOR FOR NUCLEATION ON AN INCLUSION
0.1d-6 MEAN INCLUSION DIAMETER
0.0 TOTAL VOLUME FRACTION OF INCLUSIONS
0.0 FRACTION OF EFFECTIVE INCLUSIONS
0 ANALYTICAL COMPARISON IE ADVANCED USE
0.00001 NUCLEATION FACTOR FOR PEARLITE
15000 MAXIMUM NUMBER OF PLANES
0.05 ARWID
3.0 AR
1.0 ARPEARL
```

# Bibliography

- [1] J. S. Kirkaldy, J. von Destinon-Forstmann, and R. J. Brigham. Simulation of banding in steel. *Canadian Metallurgical Quarterly*, 1:59–81, 1962.
- [2] F. G. Caballero, A. Carcía-Junceda, C. Capdevila, and C. García de Andrés. Evolution of microstructural banding during the manufacturing process of dual phase steels. *Materials Transactions*, 47:2269–2274, 2006.
- [3] G. Krauss. *Steels: Processing, Structure and Performance*. ASM International, 2005.
- [4] J. D. Verhoeven. A review of microsegregation induced banding phenomena in steels. *Journal of Materials Engineering and Performance*, 9:286–296, 2000.
- [5] J. E. Stead. *Journal of the Society of the Chemical Industry*, 33:173–84, 1913.
- [6] P. Oberhoffer. *Stahl und Eisen*, 33:1569–1574, 1913.
- [7] H. M. Howe. *The Metallography of Steel and Cast Iron*. McGraw-Hill, 1916.
- [8] G. Krauss. Solidification, segregation, and banding in carbon and alloy steels. *Metallurgical and Materials Transactions B*, 34B:781–792, 2003.
- [9] S. W. Thompson and P. R. Howell. Factors influencing ferrite/pearlite banding and origin of large pearlite nodules in a hypoeutectoid plate steel. *Materials Science and Technology*, 8:777–784, 1992.
- [10] C. F. Jaczak, D. J. Girardi, and E. S. Rowland. On banding in steel. *Transactions of the ASM*, 48:279–305, 1956.
- [11] P. G. Bastien. The mechanism of formation of banded structures. *Journal of the Iron and Steel Institute*, 187:281–291, 1957.
- [12] J. S. Kirkaldy, R. J. Brigham, H. A. Domian, and R. G. Ward. A study of banding in skelp by electron-probe microanalysis. *Canadian Metallurgical Quarterly*, 2:233–242, 1963.
- [13] E. T. Turkdogan and R. A. Grange. Microsegregation in steel. *Journal of the Iron and Steel Institute*, 208:482–494, 1970.
- [14] M. Enomoto. Simulation of solute diffusion zone formation during continuous cooling in steels containing inclusions. *Zeitschrift für Metallkunde*, 90:19–24, 1999.
- [15] L. E. Samuels. *Optical Microscopy of Steels*. ASM, 1980.
- [16] W. S. Owen, M. Cohen, and B. L. Averbach. The influence of ferrite banding on the impact properties of mild steel. *Welding Research Supplement*, pages 368–s—374–s, August 1958.

- 
- [17] C. A. Charles. Development and use of layered ferrous microstructures. *Materials Science and Technology*, 14:496–503, 1998.
- [18] Y. Tomita. Effect of modified austemper on tensile properties of 0.52% C steel. *Materials Science and Technology*, 11:994–997, 1995.
- [19] R. A. Grange. Effect of microstructural banding in steel. *Metallurgical Transactions*, 2:417–426, 1971.
- [20] A. Sakir Bor. Effect of pearlite banding on mechanical properties of hot-rolled steel plates. *ISIJ International*, 31(12):1445–1446, 1991.
- [21] P. Shanmugam and S. D. Pathak. Some studies on the impact behaviour of banded microalloyed steel. *Engineering Fracture Mechanics*, 53(6):991–1005, 1996.
- [22] Akhmad A. Korda, Y. Mutoh, Y. Miyashita, T. Sadasue, and S. L. Mannan. In situ observation of fatigue crack retardation in banded ferrite-pearlite microstructure due to crack branching. *Scripta Materialia*, 54:1835–1840, 2006.
- [23] W. A. Spitzig. Effect of sulfide inclusion morphology and pearlite banding on anisotropy of mechanical properties in normalized C-Mn steels. *Metallurgical Transactions A*, 14A:271–283, 1983.
- [24] E. Scheil. Bemerkungen zur Schichtkristallbildung. *Zeitschrift für Metallkunde*, 34:70–72, 1942.
- [25] H. D. Brody and M. C. Flemings. Solute redistribution in dendritic solidification. *Transactions of the Metallurgical Society of AIME*, 236:615–624, 1966.
- [26] M. Rappaz. Modelling of microstructure formation in solidification processes. *International Materials Reviews*, 34:93–123, 1989.
- [27] D. H. Kirkwood. Microsegregation. *Materials Science and Engineering*, 65:101–109, 1984.
- [28] M. C. M. Cornelissen. Mathematical model for solidification of multicomponent alloys. *Ironmaking and Steelmaking*, 13:204–210, 1986.
- [29] T.P. Battle. Mathematical modelling of solute segregation in solidifying materials. *International Materials Reviews*, 37:249–270, 1992.
- [30] T. Kraft and H. E. Exner. Numerische simulation der erstarrung. Teil 1: Mikrosegierungen in binären legierungen. *Zeitschrift für Metallkunde*, 87:598–611, 1996.
- [31] T. Kraft and H. E. Exner. Numerische simulation der erstarrung. Teil 2: Mikrosegierungen in ternären und höherkomponentigen legierungen. *Zeitschrift für Metallkunde*, 87:652–660, 1996.
- [32] A. Roósz, E. Halder, and H. E. Exner. Numerical-analysis of solid and liquid diffusion in microsegregation of binary-alloys. *Materials Science and Technology*, 1:1057–1062, 1985.
- [33] A. Roósz, E. Halder, and H. E. Exner. Numerical calculation of microsegregation in coarsened dendritic microstructures. *Materials Science and Technology*, 2:1149–1155, 1986.

- [34] A. A. Howe and D. H. Kirkwood. Computer prediction of microsegregation in peritectic alloy systems. *Materials Science and Technology*, 16:961–967, 2000.
- [35] W. J. Boettinger, J. A. Warren, C. Beckermann, and A. Karma. Phase-field simulation of solidification. *Annual Review of Materials Research*, 32:163–194, 2002.
- [36] T. Kraft and H. E. Exner. Numerische simulation der erstarrung. Teil 3: Vorhersage der gefügestruktur. *Zeitschrift für Metallkunde*, 88:278–290, 1997.
- [37] Q. Du and A. Jacot. A two-dimensional microsegregation model for the description of microstructure formation during solidification in multicomponent alloys: Formulation and behaviour of the model. *Acta Materialia*, 53:3479–3493, 2005.
- [38] G.S. Cole. Inhomogeneities and their control via solidification. *Metallurgical Transactions*, 2:357–370, 1971.
- [39] J.W. Martin and R.D. Doherty. *Stability of Microstructure in Metallic Systems*. Cambridge University Press, 1976.
- [40] D. Feijóo and H. E. Exner. Kritische übersicht über theoretische und experimentelle Ergebnisse zur Vergrößerung dendritischer Gefüge. *Zeitschrift für Metallkunde*, 81:654–662, 1990.
- [41] T. Z. Kattamis, J. C. Coughlin, and M. C. Flemings. Influence of coarsening on dendrite arm spacing of aluminium-copper alloys. *Transactions of the Metallurgical Society of AIME*, 239:1504–1511, 1967.
- [42] D. H. Kirkwood. A simple model for dendrite arm coarsening during solidification. *Materials Science and Engineering*, 73:L1–L4, 1985.
- [43] U. Feurer and R. Wunderlin. *Fachbericht der DGM-FB-38/667*. DGM-Informationsgesellschaft-Verlag, 1977.
- [44] G. R. Purdy and J. S. Kirkaldy. Homogenization by diffusion. *Metallurgical Transactions*, 2:371–378, 1971.
- [45] P. E. J. Rivera-Díaz-del Castillo, J. Sietsma, and S. van der Zwaag. A model for ferrite/pearlite band formation and prevention in steels. *Metallurgical and Materials Transactions A*, 35A:425–433, 2004.
- [46] W. Xu, P. E. J. Rivera-Díaz-del Castillo, and S. van der Zwaag. Ferrite/pearlite band prevention in dual phase and trip steels: Model development. *ISIJ International*, 45:380–387, 2005.
- [47] S. E. Offermann, N. H. van Dijk, M. Th. Rekveldt, J. Sietsma, and S. van der Zwaag. Ferrite/pearlite band formation in hot rolled medium carbon steel. *Materials Science and Technology*, 18:297–303, 2002.
- [48] R. Grossterlinden, R. Kawalla, U. Lotter, and H. Pircher. Formation of pearlitic banded structures in ferritic-pearlitic steels. *Steel research*, 63:331–336, 1992.
- [49] H.K.D.H. Bhadeshia. Ferrite formation in heterogeneous dual phase steels. *Scripta Metallurgica*, 17:857–860, 1983.

- 
- [50] W. A. Johnson and R. F. Mehl. Reaction kinetics in processes of nucleation and growth. *Transactions of the American Institute of Mining and Metallurgical Engineers*, 135:416–441, 1939.
- [51] M. Avrami. Kinetics of phase change I (general theory). *Journal of Chemical Physics*, 7: 1103–1112, 1939.
- [52] F. Liu, F. Sommer, C. Bos, and E. J. Mittemeijer. Analysis of solid state phase transformation kinetics: models and recipes. *International Materials Reviews*, 52(4):193–212, 2007.
- [53] S. J. Jones and H. K. D. H. Bhadeshia. Kinetics of the simultaneous decomposition of austenite into several transformation products. *Acta Metallurgica*, 45:2911–2920, 1997.
- [54] J. D. Robson and H. K. D. H. Bhadeshia. Modelling precipitation sequences in power plant steels. Part 1 – Kinetic theory. *Materials Science and Technology*, 13:631–639, 1997.
- [55] S. J. Jones and H. K. D. H. Bhadeshia. Competitive formation of inter- and intragranularly nucleated ferrite. *Metallurgical and Materials Transactions A*, 28A:2005–2013, 1997.
- [56] J. W. Christian. *Theory of Transformations in Metals and Alloys*. Pergamon Press, Oxford, 2nd edition, 1975.
- [57] H. K. D. H. Bhadeshia, L.-E. Svensson, and B. Grefott. *Welding Metallurgy of Structural Steels*, pages 517–530. TMS-AIME, 1987.
- [58] R. Triverdi and G. R. Pound. *Journal of Applied Physics*, 38:3569, 1967.
- [59] H. K. D. H. Bhadeshia. *Acta Metallurgica*, 29:1117, 1981.
- [60] R. Triverdi. *Metallurgical Transactions*, 1:921, 1970.
- [61] G. I. Rees and H. K. D. H. Bhadeshia. *Materials Science and Technology*, 8:985, 1992.
- [62] M. Hillert. *Jernkontorets Ann.*, 141:757, 1957.
- [63] M. Takahashi. *Reaustenitisation from Bainite in steels*. PhD thesis, Cambridge University, 1992.
- [64] S. J. Jones and H. K. D. H. Bhadeshia. Program STRUCTURE on the Materials Algorithm Project web site, last accessed 15. August 2007. URL <http://www.msm.cam.ac.uk/map/steel/programs/structure.html>.
- [65] S. V. Parker. *Modelling of Phase Transformations in Hot-Rolled Steels*. PhD thesis, University of Cambridge, 1997.
- [66] S. J. Jones and H. K. D. H. Bhadeshia. Kinetics of the widmanstätten ferrite transformation. In K. Otsuka, K. Inoue, K. Mukherjee and H. Chen, editors, *Displacive Phase Transformations and their Applications in Materials Engineering*, pages 419–426. The Minerals, Metals and Materials Society, Warrendale, Pennsylvania, USA, 1998.